

Feynman Diagrams for Matter Wave Interferometry

Jonah Glick*

*Department of Physics and Astronomy and Center for Fundamental Physics,
Northwestern University, Evanston, Illinois, USA and
Fermi National Accelerator Laboratory, Batavia, Illinois, USA*

Tim Kovachy

*Department of Physics and Astronomy and Center for Fundamental Physics,
Northwestern University, Evanston, Illinois, USA*

(Dated: November 25, 2025)

We introduce a new theoretical framework based on Feynman diagrams to compute phase shifts in matter wave interferometry. The method allows for analytic computation of higher order quantum corrections, beyond the traditional semi-classical approximation. These additional terms depend on the finite size of the initial matter wavefunction and/or have higher order dependence on \hbar . We apply the method to compute the response of matter wave interferometers to power law potentials and potentials with an arbitrary spatial dependence. The analytic expressions are validated by comparing to numerical simulations, and estimates are provided for the scale of the quantum corrections to the phase shift response to the gravitational field of the earth, anharmonic trapping potentials, and gravitational fields from local proof masses. We also find that for certain experimentally feasible parameters, these corrections are large enough to be measured, and could lead to systematic errors if they are not mitigated. We find that to first order in spatially dependent potential, quantum corrections vanish when the initial matter wavepacket has spherical symmetry and the potential satisfies Laplace's equation. We anticipate these quantum corrections will be especially important for trapped matter wave interferometers and for free-space matter wave interferometers in the presence of proof masses. These interferometers are becoming increasingly sensitive tools for mobile inertial sensing, gravity surveying, tests of gravity and its interplay with quantum mechanics, and searches for dark energy.

I. INTRODUCTION

Matter wave interferometry is a powerful tool for precision sensing and tests of fundamental physics. It is employed in a wide range of applications, including inertial navigation [1–4], gravity surveying [5–8], geodesy and geophysical studies [9, 10], tests of the equivalence principle and searches for fifth forces [11–24], measurements of Newton's gravitational constant [25–27] and the fine structure constant [28, 29], searches for dark energy [30, 31], searches for dark matter [32–40], gravitational wave detection [8, 33, 34, 39–52], and tests of quantum mechanics and its interplay with gravity [53–64].

The calculation of the differential phase accumulated between two arms of a matter wave interferometer due to spatially varying external potentials has traditionally relied on a semi-classical approximation [9, 46, 65–70]. This approximation neglects the finite spatial extent of an individual arm of the matter wavefunction and excludes contributions to the phase shift at orders of \hbar higher than \hbar^{-1} [71]. While numerical simulation tools have been developed that do not rely on semi-classical approximations [72], analytical expressions have been highly valuable for understanding scalings of various contributions to the phase shift in order to guide experimental design and analysis [9, 66, 67].

We adapt the mathematical tools of quantum field theory (QFT) to introduce a Feynman diagram based approach to analytically computing the phase shift in a matter wave interferometer which incorporates higher-order quantum corrections from the finite extent of a matter wavefunction, and higher order terms in \hbar . Our approach is complementary to analyses based on Wigner function [73] or Magnus/Dyson series [74–76] formalisms, and it provides a structured framework for higher-order corrections, similar to the way Feynman diagrams are used in perturbative quantum field theory. In field-theoretic treatments, Feynman diagrams have been used to estimate phase shifts from hypothetical scalar fields [77–79]. Here, we instead apply diagrammatic methods within a purely quantum-mechanical framework.

We find higher order quantum corrections to be especially relevant in trapped matter wave interferometers with small anharmonicities, where external potentials exhibit strong position dependence. This new diagrammatic tool can be used to generate analytic estimates of these corrections in interferometers confined to magnetic [80–84] and optical [85–96] potentials, which commonly consist of anharmonicities that can induce beyond-semi-classical phase shifts. Trapped interferometers are emerging as powerful tools for applications including mobile inertial sensing and gravity surveying [83, 85–91, 97], searches for dark energy and tests of gravity at short distances [92], and tests of quantum gravity [63]. Higher order quantum corrections will also be relevant to free-space interferometers that measure gravitational effects

* jonah.glick@gmail.com

from local proof masses, like those aimed at obtaining precision measurements of Newton’s gravitational constant [25–27, 73] and testing the gravitational inverse square law to search for new fundamental interactions [11, 24]. As illustrative case studies, we identify examples in which these quantum corrections would yield a measurable effect in experimentally realistic trapped and proof-mass-style matter wave interferometers.

The paper is organized as follows: In Sec. II, we introduce the framework by reviewing the relevant background from QFT (Sec. II A), introducing one way to compute phase shifts in matter wave interferometry (Sec. II B), merge the two ideas to compute phase shifts with Feynman diagrams (Sec. II C), then make connections to the traditional semi-classical approach to computing phase shifts (Sec. II D). In Sec. III we apply the diagrammatic method to compute phase shifts under power law potentials. We investigate the validity of these expression by comparing to numerical evaluations of the phase shift in a certain parameter space, propagating wavepackets with the split step method [98]. We then take the analytic terms which emerge from the diagrammatic framework and use them to evaluate phase shifts from gravity gradients of the earth (Sec. III A), and for interferometers confined to anharmonic traps (Sec. III B). In Sec. IV, we sum over an infinite number of diagrams to produce an analytic expression for the phase shift response to an external potential with arbitrary spatial dependence, and apply the expression to estimate quantum corrections to the phase shift for a proof-mass style experiment.

II. FRAMEWORK FOR PHASE SHIFT CALCULATIONS

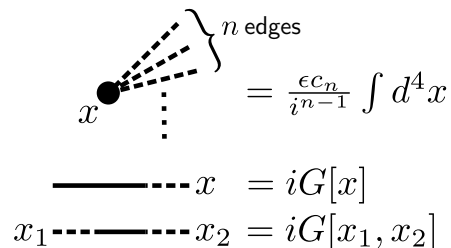
A. QFT Background

Here we express the key mathematical identity from QFT which we will apply to computing phase shifts in matter wave interferometry. Consider a scalar field theory with Lagrangian density $\mathcal{L} = \mathcal{L}_0 + \epsilon\mathcal{L}_1 + J\varphi$, where $\mathcal{L}_0 = -\frac{1}{2}\partial^\mu\varphi\partial_\mu\varphi - \frac{1}{2}m^2\varphi^2$ is the ‘free’ component of the Lagrangian density, \mathcal{L}_1 is a contribution that is third order or higher in φ , J is a source term, and ϵ is a perturbative parameter we can use to keep track of the orders of expansion. The ground state to ground state amplitude in this theory with a nonzero source term can be written as

$$\begin{aligned} \langle 0|0\rangle_J &= \int \mathcal{D}\varphi e^{i\int d^4x (\mathcal{L}_0 + \epsilon\mathcal{L}_1 + J\varphi)} \\ &= e^{i\int d^4x \epsilon\mathcal{L}_1 \left[\frac{1}{i}\frac{\delta}{\delta J(x)}\right]} \int \mathcal{D}\varphi e^{i\int d^4x (\mathcal{L}_0 + J\varphi)} \\ &= e^{i\int d^4x \epsilon\mathcal{L}_1 \left[\frac{1}{i}\frac{\delta}{\delta J(x)}\right]} e^{\frac{i}{2}\int d^4x_1 \int d^4x_2 J[x_1]G[x_1, x_2]J[x_2]} \end{aligned} \quad (1)$$

where for the second equality, we have made use of a well-

established trick in QFT to take the nonlinear component of the Lagrangian density outside of the path integral by replacing its argument in φ with functional derivatives with respect to the source term J . The last equality highlights that after taking the nonlinear component of the Lagrangian density outside of the integrand, the path integral can be solved in closed form, where the *propagator* G is symmetric under an exchange of its arguments, $G[x_1, x_2] = G[x_2, x_1]$ [99–101]. For simplicity, we take $\hbar = 1$. One can solve for $\langle 0|0\rangle_J$ perturbatively in ϵ by Taylor expanding both exponentials in the last equality of Eq. 1 and applying the functional derivatives of the first exponential to the functionals of the second (see Appendix B). It is productive to organize the terms of this expansion with diagrams. The philosophy of Feynman diagrams is to ascribe value to the edges and vertices which compose a diagram so that a single diagram corresponds to a single term in the Taylor series expansion of Eq. 1. The four step process of diagrammatically computing the n^{th} order expansion of $\langle 0|0\rangle_J$ in ϵ is to 1. compute the value of the edges and vertices, 2. compose all n -vertex diagrams, 3. evaluate the integrals associated with the diagrams, and 4. sum the diagrams together. In the case of perturbatively evaluating $\langle 0|0\rangle_J$ in ϵ , the value of the edges and vertices can be written as

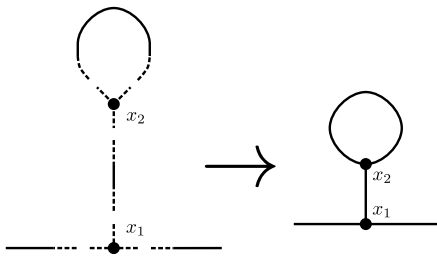


$$\begin{aligned} \text{Vertex } x \text{ with } n \text{ edges} &= \frac{\epsilon c_n}{i^{n-1}} \int d^4 x \\ \text{Edge } x &= iG[x] \\ \text{Edge } x_1 \text{---} x_2 &= iG[x_1, x_2] \end{aligned}$$

where $G[x] = \int d^4x' J[x']G[x', x]$, c_n is the n th order Taylor series coefficient in the expansion of \mathcal{L}_1 , $\mathcal{L}_1 = \sum_{i=0}^{\infty} \frac{1}{n!} c_n \varphi^n$, dashed lines correspond to connections of an edge and vertex (see example below), and x_i is the label of the vertex. The key identity we will be leveraging when we apply this formalism to phase shift calculations in matter wave interferometry is that the ground state to ground state amplitude can then be written as [99]

$$\langle 0|0\rangle_J = e^{\text{sum of all connected diagrams}} \quad (2)$$

where the value of each diagram is weighted by the inverse of the number of automorphisms of the diagram, also called the *symmetry factor*. As an example, consider an interaction $\mathcal{L}_1 = \frac{c_3}{3!} \varphi^3$. One of the diagrams which would contribute to the ϵ^2 order expansion of $\text{Log}[\langle 0|0\rangle_J]$ under this nonlinearity is



where according to the above values ascribed to the vertices and edges this diagram has value

$$\frac{1}{4} \left(\frac{\epsilon c_3}{i^{3-1}} \right)^2 \int d^4 x_1 \int d^4 x_2 (i)^4 G[x_1]^2 G[x_1, x_2] G[x_2, x_2]$$

and the factor of $1/4$ comes from the inverse of the symmetry factor of the diagram. Further details can be found in [99–101].

B. Phase Shift Calculation Background

Here we will outline an approach to leveraging Eq. 2 to compute phase shifts in matter wave interferometry. Consider a system with one spatial dimension, x , and one temporal dimension, t . The interferometer is composed of two arms which are represented by wavefunctions $\psi_1[x, t]$ and $\psi_2[x, t]$ respectively (see Fig. 1). We take these wavefunctions to arrive at the same output port of the interferometer. For simplicity, we assume the operations which split, re-direct, and interfere the two arms occur instantaneously. Take the first beamsplitter operation to be at time $t = 0$, and the time between laser pulses to be T in a Mach-Zehnder pulse sequence. Let us define t_i to be some *initial* time before the first beamsplitter operation $t_i < 0$, and t_f to be a *final* time after the second beamsplitter operation $t_f > 2T$. The interferometer contrast C and phase shift $\Delta\phi$ under spatial averaging can be expressed as

$$\frac{1}{2} \left(1 + C \cos[\Delta\phi] \right) = \frac{1}{4} \int_{-\infty}^{\infty} dx_f |\psi_1[x_f, t_f] + \psi_2[x_f, t_f]|^2$$

where we normalize the wavefunctions ψ_1 and ψ_2 so that the total probability associated with each is 1. The factor of $1/4$ comes from two factors of $1/\sqrt{2}$ from the first and final 50:50 beamsplitters, which are then squared under the modulus squared operation. Expanding out this equation, we have

$$\begin{aligned} & \frac{1}{4} + \frac{1}{4} + \frac{C}{4} e^{i\Delta\phi} + \frac{C}{4} e^{-i\Delta\phi} \\ &= \int_{-\infty}^{\infty} dx_b \left(\frac{1}{4} |\psi_1|^2 + \frac{1}{4} |\psi_2|^2 + \frac{1}{4} \psi_1 \psi_2^* + \frac{1}{4} \psi_1^* \psi_2 \right) \\ &= \frac{1}{4} + \frac{1}{4} + \int_{-\infty}^{\infty} dx_b \left(\frac{1}{4} \psi_1 \psi_2^* + \frac{1}{4} \psi_1^* \psi_2 \right) \end{aligned}$$

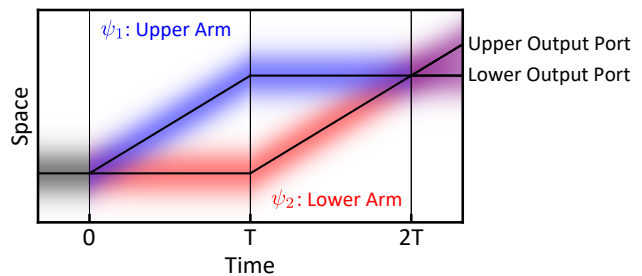


FIG. 1. A Mach-Zehnder interferometer sequence. Black solid lines denote classical trajectories, the blue corresponds to the wavepacket of the upper interferometer arm and the red corresponds to the lower interferometer arm. These arms are represented by wavefunctions ψ_1 and ψ_2 respectively. The gray density plot corresponds to the wavepacket before the first beamsplitter and the purple denote the interference of the blue and red interferometer arms. The vertical lines denote the times of the instantaneous beamsplitter and mirror operations.

Then comparing cross terms in a manner consistent with the sign conventions of Ref. [66] results in

$$C e^{i\Delta\phi} = \int_{-\infty}^{\infty} dx_f \psi_1[x_f, t_f] \psi_2^*[x_f, t_f] \quad (3)$$

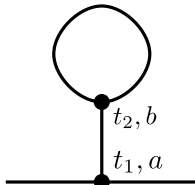
C. Computing Phase Shifts with Feynman Diagrams

We now derive an expression for the right hand side of Eq. 3 which will be structurally very similar to that of the last equality in Eq. 1 and which will enable us to diagrammatically compute phase shifts in matter wave interferometry. The amplitude associated with a trajectory which is located at position x_i at time t_i and located at position x_f at a later time t_f can be written following the Feynman path integral approach [102] as

$$K[x_f, t_f; x_i, t_i] = \int \mathcal{D}x[t] e^{\frac{i}{\hbar} S[x, t]}$$

where S is the action associated with a classical path $x[t]$, and the path integral is performed over all paths which start at position x_i and time t_i and arrive at position x_f and time t_f . For the following sections of the paper, expressions will explicitly include dependence on \hbar . We can call this amplitude K the kernel propagator. Consider a system with Lagrangian $L = L_0[\dot{x}, x, t] + \epsilon L_1[x] + J[t]x$, where L_0 corresponds to the ‘free’ Lagrangian which consists of a kinetic energy term (with second order dependence on \dot{x}) and potential energy terms (containing only second order or lower dependence on x), L_1 consists of terms of any order in x , $J[t]$ is an external force, and ϵ is a perturbative parameter to keep track of the orders of expansion. This amplitude can be written as

where the delta functions are Kronecker delta functions, and c_n is the n^{th} order Taylor series coefficient of $L_1[x]$. The focus of this paper will be on using Eq. 2 to solve Eq. 3 perturbatively in spatial potentials which render the equations of motion nonlinear. As an example, consider a system with a nonlinear potential $L_1 = \frac{\epsilon_3}{3!}x^3$. To compute a second order correction to the phase shift under this nonlinearity in the external potential, it will be productive to write down and sum all diagrams with two 3-point vertices. In parallel with the example in Sec. II A, one such diagram can be written as



where, following the rules above, the value of the diagram can be written as

$$\begin{aligned} & \frac{1}{4}\lambda_a^3\lambda_b^3(c_3)^2 \int_{t_i}^{t_f} dt_1 \int_{t_i}^{t_f} dt_2 G_a[t_1]^2 G_{ab}[t_1, t_2] G_{bb}[t_2, t_2] \\ &= \frac{(\epsilon c_3)^2 \hbar^4}{4} \int_{t_i}^{t_f} dt_1 \int_{t_i}^{t_f} dt_2 \left(G_1[t_1]^2 G_{11}[t_1, t_2] G_{11}[t_2, t_2] \right. \\ & \quad + G_1[t_1]^2 G_{12}[t_1, t_2] G_{22}[t_2, t_2] \\ & \quad + G_2[t_1]^2 G_{21}[t_1, t_2] G_{11}[t_2, t_2] \\ & \quad \left. + G_2[t_1]^2 G_{22}[t_1, t_2] G_{22}[t_2, t_2] \right) \end{aligned}$$

where we use Eq. 8 and sum over Latin indices. Referencing Eq. 7, the contribution to the phase is then given by the imaginary part of this term, and the quantum corrections to the interferometer contrast are determined by taking the real part.

We now generalize the diagrammatic phase shift rules to three spatial dimensions. In 1D, vertices are labeled by a time variable t_i and an interferometer arm index $a = 1, 2$. The 3D diagrams follow the same procedure, except that each edge now also carries a label to index the cartesian dimensions. One notationally convenient way to write the diagram rules in 3D is to denote these new labels with Greek indices, which run from 1 to 3 for each of the three spatial dimensions. An alternate way to write out the diagram rules in 3D is to explicitly label the diagram edges with the cartesian coordinate, and write out all the permutations over the possible cartesian coordinate labels as independent diagrams. This second approach is explored in more detail in supplement Sec. D). For the purposes of this paper, we assume a separable form for the unperturbed Lagrangian L_0 (i.e. $L_0[\dot{x}, x, \dot{y}, y, \dot{z}, z] = L_x[\dot{x}, x] + L_y[\dot{y}, y] + L_z[\dot{z}, z]$). In three spatial dimensions, the value of the different components of the diagrams can be written as

$$\begin{aligned} & \left. \begin{array}{l} \alpha_1 \\ \alpha_2 \\ \alpha_3 \\ \vdots \end{array} \right\} n \text{ edges} \\ & t, a \bullet \quad = -m \Gamma_{\alpha_1 \alpha_2 \dots \alpha_n}^{(n-1)} \lambda_a^n \int_{t_i}^{t_f} dt \\ & \text{---} \alpha t, a = G_a^\alpha[t] \\ & t_1, a \text{---} \alpha \text{---} \beta t_2, b = G_{ab}^{\alpha\beta}[t_1, t_2] \end{aligned}$$

where $G_a^\alpha[t] = \int_{t_i}^{t_f} dt' J_{a'}^\alpha[t'] G_{a'a}^{\alpha'}[t', t_i]$, and $\Gamma_{\alpha_1 \alpha_2 \dots \alpha_n}^{(n-1)}$ are the coefficients of the 3D Taylor series expansion of L_1 . Here we are adopting the notation of Ref. [75] for the coefficients of the Taylor series expansion.

$$L_1[x, y, z] = -m \sum_{n=0}^{\infty} \frac{1}{n!} \Gamma_{\alpha_1 \alpha_2 \dots \alpha_n}^{(n-1)} r_{\alpha_1} r_{\alpha_2} \dots r_{\alpha_n}$$

Where summation of repeated Greek and Latin indices is assumed ($\alpha = 1, 2, 3$), and $r_1 = x, r_2 = y, r_3 = z$. The value of the functions $G_a^\alpha[t]$ and $G_{ab}^{\alpha\beta}[t_1, t_2]$ depend on the interferometer laser sequence, as well as the form of the unperturbed Lagrangian. Specific values for these diagram values are given in example calculations in Sec. III.

D. Connection to Traditional Semi-classical Framework

The traditional semi-classical approach to computing phase shifts involves separating the contributions of the phase into three parts : 1. a laser phase $\Delta\phi_{\text{laser}}$, which has to do with the imprint of the laser phase onto the matter waves, 2. a propagation phase $\Delta\phi_{\text{prop}}$, which has to do with the differential phase accumulated during the free propagation of the two arms under the spatially varying potential, and 3. a separation phase $\Delta\phi_{\text{sep}}$, which has to do with the two arms of the interferometer within the same output port not being perfectly overlapped with one another under spatial averaging. The total phase shift $\Delta\phi$ is expressed as a sum of these three components, $\Delta\phi = \Delta\phi_{\text{laser}} + \Delta\phi_{\text{prop}} + \Delta\phi_{\text{sep}}$ [9, 66].

In the diagram formalism, the propagation phase is associated with the convolution of wavepackets with kernels K , the separation phase is associated with the spatial averaging integrals over x_f in Eq. 6, and the laser phase is encoded in the external force term $J[t]$. In the semi-classical formalism, the laser phase associated with an individual interferometer arm can be written as $\sum_j \pm k_x x_{\text{cl}}[t_j]$ where the sum is over all kicks to the classical trajectory, $x_{\text{cl}}[t]$, indexed by j . Kick j occurs at time t_j , and k_x is the wavenumber of the light causing the kick. The sign of the phase imprint depends on the direction of the kick. In the limit of instantaneous matter-optics pulses, where $J[t]$ consists of delta functions in time (see for example Eq. 10 and Eq. 12), the laser kick can be thought of as applying an instantaneous

phase shear across the wavepacket, akin to applying the operator $e^{\pm i \frac{p}{\hbar} v_r \cdot \hat{x}}$ to the wavepacket at the time of the pulse, where $v_r = \hbar k_x / m$ is the recoil velocity associated with the photon kick. The sign of the phase gradient depends on the direction of the kick. The phase gradient across the wavepacket imparts a momentum kick, and the mean phase imprinted onto the wavepacket on top of the gradient has the form $\pm k_x x_{\text{cl}}[t_j]$, as in the semi-classical formalism

It has been shown using Ehrenfest's theorem that when the external potential is at most quadratic in x , the interferometer phase shift is fully captured by the semiclassical approximation: there are no higher-order \hbar corrections, and no contributions from the finite spatial extent of the wavepacket [66]. There is a natural way to see this feature within the diagram formalism. If there is no harmonic component included in L_0 , so that harmonic contributions to the Lagrangian are treated perturbatively, the one-vertex tree-level (loop-free) diagrams reproduce the semi-classical solution to first order in the perturbative potential. Higher-order quantum corrections for these one-vertex diagrams arise from loops (see Tab. I, where the leading order quantum correction comes from a diagram with a loop). Vertices and internal edges carry no dependence on $J[t]$, only external edges encode information about the laser kicks. 'Bubble' diagrams, which have no external edges, therefore carry no information about the interaction between the matter wave and the interferometer laser. If there is no interaction with the interferometer laser, there can be no phase shift, so these bubble diagrams always sum to zero [104]. The fact that higher order than quadratic terms are required to induce beyond-semi-classical corrections to the phase shift arises in the diagram formalism by the fact that it is not possible to construct a diagram with one loop and at least one external edge using only a 2-point vertex. Only with a 3-point vertex (a cubic term in the Lagrangian) can a non-zero loop-level diagram be constructed, leading to higher order quantum corrections. In this context, an n -vertex diagram is a diagram with n vertices, and an n -point vertex is a vertex with n edges connected to it.

III. APPLICATION: COMPUTING PHASE SHIFTS FROM POWER LAW POTENTIALS

One can choose whether or not to include the harmonic component as part of the unperturbed component of the Lagrangian L_0 , or to include it as part of the perturbed component. In this section, we explore both options. When the harmonic component is small, it can be more convenient to treat it perturbatively. Neglecting it in L_0 leads to simpler integrands and therefore time integrals that are easier to evaluate. The trade-off is that one must then explicitly compute diagrams with two-point vertices associated with the perturbative treatment of the harmonic term. Conversely, when the interferometer is operated in a harmonic trap, or more generally when

the harmonic term is not small, and many orders of the harmonic component are required, a perturbative treatment of the harmonic term can require summing a large number of diagrams to account for all relevant two-point vertices. In these cases, it can be simpler to absorb the harmonic component into the unperturbed Lagrangian and treat only the n -point vertices with $n \geq 3$ as perturbations. This avoids the need for a high-order diagrammatic expansion in the trap frequency at the cost of a slightly more complicated unperturbed solution.

A. Treating Harmonic Terms Perturbatively

1. Diagram Values

In this section we use the rules outlined in Sec. II B to evaluate the value of diagram elements for a free unperturbed potential, and use the diagrams to analytically compute phase shifts for matter wave interferometers subject to an external potential expressed as a power series in position. Consider a Lagrangian of the form $L = L_0 + \epsilon L_1 + \mathbf{J}[t] \cdot \mathbf{r}$, where

$$\begin{aligned} L_0 &= \frac{m}{2} (\dot{x}^2 + \dot{y}^2 + \dot{z}^2) - mgz \\ L_1 &= - \left(\frac{m}{2} (T_{xx}x^2 + T_{yy}y^2 + T_{zz}z^2) \right. \\ &\quad + \frac{m}{3!} (3Q_{xxz}x^2z + 3Q_{yyz}y^2z + Q_{zzz}z^3) \\ &\quad \left. + \frac{m}{4!} S_{zzzz}z^4 \right) \end{aligned} \quad (9)$$

where T_{ij} , Q_{ijk} , and S_{ijkl} correspond to coefficients of the Taylor series expansion in space of the Earth's gravitational field about the surface of the earth, where we assume a spherical earth with homogeneous mass density, and z is the axis of the interferometer. More generally, these coefficients could correspond to the Taylor expansion of any spatially varying potential, such as that generated by a dipole beam, or nonuniform magnetic fields. With $L_1 = 0$, the interferometer phase can be computed by evaluating the 3D version of the spatial integrals of Sec II B, which results in

$$\begin{aligned} G_{11}^{\alpha\alpha}[t_j, t_k] &= \frac{1}{2m\hbar} \left(-\beta_\alpha t_j t_k - \frac{1}{\beta_\alpha} + i|t_j - t_k| \right) \\ G_{12}^{\alpha\alpha}[t_j, t_k] &= \frac{1}{2m\hbar} \left(\beta_\alpha t_j t_k + \frac{1}{\beta_\alpha} + i(t_j - t_k) \right) \\ G_{21}^{\alpha\alpha}[t_j, t_k] &= \frac{1}{2m\hbar} \left(\beta_\alpha t_j t_k + \frac{1}{\beta_\alpha} - i(t_j - t_k) \right) \\ G_{22}^{\alpha\alpha}[t_j, t_k] &= \frac{1}{2m\hbar} \left(-\beta_\alpha t_j t_k - \frac{1}{\beta_\alpha} - i|t_j - t_k| \right) \end{aligned}$$

where $\beta_\alpha = 2\hbar/m(w_{0,\alpha})^2$, where $w_{0,1}, w_{0,2}, w_{0,3}$ are the initial wavepacket waists in the x , y , and z dimensions

respectively. This calculation is done in detail in 1D in Appendix A, and extended to 3D in Appendix C. For a Mach-Zehnder interferometer, with an interferometer beam oriented along the z -axis, the external force term has the form

$$\frac{J_a^3[t]}{m} = -g + \begin{cases} v_r \delta[t-0] - v_r \delta[t-T], & a = 1 \\ v_r \delta[t-T] - v_r \delta[t-2T], & a = 2 \end{cases} \quad (10)$$

corresponding to interference between the two arms in the ‘lower’ output port of the interferometer referencing Fig. 1. J_1^3 corresponds to the kicks on the ‘upper’ arm of the interferometer, and J_2^3 corresponds to the kicks on the ‘lower’ arm. The superscript 3 denotes the z axis, and laser kicks along the x and y axes can be captured by modifying the values of $J_a^1[t]$ and $J_a^2[t]$ respectively. For the calculations we will do in this section, we will take $J_a^1[t]$ and $J_a^2[t] = 0$. Alternate pulse sequences can be computed by adding/modifying terms that are proportional to the recoil velocity v_r . In this system, the value of the external vertices can be expressed in terms of the semi-classical trajectories of the interferometer arms

$$\begin{aligned} G_a^1[t] &= (-1)^{a+1} \frac{i}{\hbar} x_{\text{cl},a}^{(0)}[t] \\ G_a^2[t] &= (-1)^{a+1} \frac{i}{\hbar} y_{\text{cl},a}^{(0)}[t] \\ G_a^3[t] &= (-1)^{a+1} \frac{i}{\hbar} z_{\text{cl},a}^{(0)}[t] \end{aligned} \quad (11)$$

where $z_{\text{cl},1}^{(0)}[t]$ and $z_{\text{cl},2}^{(0)}[t]$ are the unperturbed classical trajectories of the two interferometer arms (indexed by a) along z , which evolve under the Lagrangian L_0 . For the calculations we will perform in this section, the deflections of the semiclassical trajectories transverse to the interferometer axis will be zero, such that $x_{\text{cl},a}^{(0)}[t] = y_{\text{cl},a}^{(0)}[t] = 0$. Eq. 11 holds even when we account for a nonzero initial position z_0 and velocity v_z of the classical trajectory. See Appendix A for more details. We now use these rules to compute phase shifts under power law potentials.

2. Validating with Numerics in 1D

Here we demonstrate agreement between the diagrammatic approach to computing phase shifts and an *ab-initio* numerical evaluation of the phase shift which accounts for the contributions that emerge from the finite-size nature of the matter wavepacket. Consider the Lagrangian of Eq. 9 with $x = y = T_{zz} = S_{zzzz} = 0$ and no higher order terms in x , y , or z . We leverage the split-step [98] approach in one spatial dimension (z) to numerically time evolve matter wavepackets in this power-law potential. We independently time evolve the two wavepackets associated with the two interferometer arms.

The instantaneous laser kicks are performed by applying linear phase gradients across the two wavefunctions between discrete time steps. The phase is then extracted by performing a discrete sum over spatial coordinates to evaluate $P_{\text{lower}}[\phi_b]$, the population in the ‘lower’ output port, for different values of the final beamsplitter phase ϕ_b , $P_{\text{lower}}[\phi] = \int_{-\infty}^{\infty} dz_f |\psi_1[z_f, t_f] + \psi_2[z_f, t_f] e^{-i\phi_b}|^2$ for 63 evenly spaced values of ϕ between 0 and 2π at the time immediately following the final beamsplitter, then fitting P_{lower} to the function $\frac{1}{2}(1 + C \cos[\Delta\phi + \phi_b])$ with fit parameters C , the interferometer contrast, and $\Delta\phi$, the interferometer phase shift. Here ψ_1 is the wavefunction which corresponds to the ‘upper’ interferometer arm in Fig. 1.

We run these simulations to verify the mathematical approach, and use unphysical parameters (e.g. larger values of \hbar) to amplify quantum corrections and reduce computational complexity. Realistic physical parameters require high spatial-temporal resolution for accuracy, which increases computation time. These simulations do not represent expected phase shifts, but serve to validate the analytic terms which come out of the diagrammatic formalism. The analytic terms are then used to estimate realistic phase shifts (see Sections III A 3, III B 3, and IV C). Figure 2 plots the interferometer phase shift as a function of interrogation time under this power-law potential computed in three different ways : 1. numerically (black dots), 2. using the traditional semi-classical approach expanded to second order in Q_{zzz} (dashed red line), and 3. using the diagrammatic approach, shown separately to first order in Q_{zzz} (dashed gray line) and to second order in Q_{zzz} (solid gray line). The two contributing diagrams to first order in Q_{zzz} , along with the three diagrams that contribute at second order in Q_{zzz} are indicated in the bottom left corner of panel (a). Simulation parameters are indicated in the caption. In this parameter space, the terms that emerge from the diagrammatic calculator have strong agreement with the output of the split-step numerics, whereas the semi-classical approach deviates more strongly from the numerical results. Panel (b) of Fig. 2 displays the classical trajectories of the two interferometer arms (black lines) for a $T = 100$ ms interferometer sequence. The gray density plot indicates the wavepacket waist before the first beamsplitter operation at time $t = 0$. The blue density plot indicates the wavepacket associated with the ‘upper’ interferometer arm, and the red wavepacket corresponds to the ‘lower’ interferometer arm. The diagrammatic approach re-produces the terms which emerge from the semi-classical solver, and produce new terms associated with higher order quantum corrections. Let us define the interferometer phase shift $\Delta\phi$ as a sum of the semi-classically accumulated phase and quantum corrections, $\Delta\phi = \Delta\phi_{\text{cl}} + \Delta\phi_{\text{qu}}$. The terms which emerge from the diagrammatic calculation but which do not emerge from the semi-classical calculation to second order in Q_{zzz} are

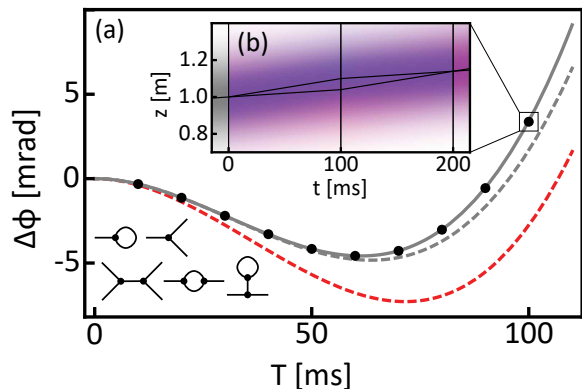


FIG. 2. (a) Phase shifts under the Lagrangian $L = m\dot{z}^2/2 - mgz - mQ_{zzz}z^3/3!$ as computed numerically (black dots), via the traditional semi-classical formalism to second order in Q_{zzz} (red dashed line), and computed diagrammatically to first order in Q_{zzz} (gray dashed line), and to second order in Q_{zzz} (gray solid line). The diagrams which contribute to the first and second order corrections in Q_{zzz} are indicated in the bottom left hand side. The simulation parameters are as follows, with each parameter expressed in SI units: $\hbar/m = 10^{-2}$, $w_0 = 0.3$, $v_r = 0.6$, $v_z = 0.4$, $z_0 = 1$, $g = 0.52$, $Q_{zzz} = -0.9$, $T_{zz} = S_{zzzz} = 0$, and no higher order potential terms. The split step numerics were done with spatial resolution $\Delta z = 2.5$ mm, a temporal resolution of $\Delta t = 0.5$ ms, and a grid centered at $z = 0$ with a size of 4 m. (b) The span of the two interferometer arms for $T = 100$ ms. The gray density plot indicates the width of the wavefunction before the first beamsplitter. The first beamsplitter operation splits the wavefunction into an upper arm (blue) and lower arm (red). The final beamsplitter then interferes the two arms (purple). The classical trajectories are indicated with solid black lines.

$$\begin{aligned} \Delta\phi_{\text{qu}} = & -Q_{zzz}v_r \left(\frac{1}{4\beta_3}T^2 + \frac{7\beta_3}{24}T^4 \right) \\ & + Q_{zzz}^2v_r \left(\frac{7}{16\beta_3}z_0T^4 + \frac{5}{32\beta_3}v_rT^5 + \frac{5}{16\beta_3}v_zT^5 \right. \\ & \quad - \frac{31}{180\beta_3}gT^6 + \frac{31\beta_3}{144}z_0T^6 + \frac{3\beta_3}{32}v_rT^7 \\ & \quad \left. + \frac{3\beta_3}{16}v_zT^7 - \frac{1397\beta_3}{13440}gT^8 \right) \\ & + \mathcal{O}[Q_{zzz}^3] \end{aligned}$$

These quantum correction terms are the source of the disagreement between the semi-classically calculated phase shift and the diagrammatically calculated phase shift in Fig. 2. In order to emphasize the utility of the diagrammatic method for computing higher order corrections to atom interferometer phase shifts, we chose a numerical parameters in Fig. 2 so that the second order Q_{zzz} contributions can be numerically resolved.

3. 3D Calculation of Higher Order Quantum Corrections under Gravity Gradients of the Earth

To explore the extent to which these higher order quantum corrections under power law potentials associated with the spherical nature of the Earth could be measured with a state-of-the-art matter wave interferometer, we take the analytic expressions that come out of the diagrammatic formalism, and plug in typical operating parameters (parameters indicated in the caption of Table I). In Table I, we rank each of the terms that come out of this calculation in order of the size of their contribution to the interferometer phase shift, with the higher order quantum correction terms highlighted gray.

The largest term not captured by the semiclassical formalism has a relative magnitude of roughly one part in 10^{20} with respect to the largest overall $-kgT^2$ term, which would be difficult to resolve experimentally with state-of-the-art atom interferometers. However, the numerical values of the Taylor series coefficients used above assume perfectly spherical earth with homogeneous mass density, and may differ significantly from realistic values. More realistic coefficients (accounting for the non-spherical nature of the earth, its inhomogeneous mass density, nearby structures, sea level variations, and other sources of gravitational potentials) could be orders of magnitude larger than those considered here [105, 106]. We emphasize that the calculation presented here is intended as a demonstration of the method for computing quantum corrections to power-law potentials in general. In practice, the true coefficients (T_{ij} , Q_{ijk} , ...) would need to be measured at the site of the interferometer.

It is important to carry out these calculations in three dimensions. Even though the semiclassical trajectories do not deflect in the directions transverse to the interferometer axis (i.e. the classical paths lie entirely along z), quantum corrections still depend on the transverse gravity gradients. For the potentials considered in Table I, if the initial wavepacket is spherically symmetric ($w_{0,1} = w_{0,2} = w_{0,3}$), then the value of the 1-loop 3-point vertex diagram of Table I vanishes: the terms proportional to Q_{xxz} (term 26) and Q_{yyz} (term 27) cancel with the corresponding Q_{zzz} contribution (term 23). This cancellation was noted in Ref. [75]. The diagrammatic formalism can be used to prove that, more generally, if the wavepacket is prepared with spherical symmetry, then the first-order quantum corrections to the semiclassical approximation vanish for any external potential $V[\mathbf{r}]$ that satisfies Laplace's equation, $\nabla^2 V[\mathbf{r}] = 0$. We work out this result explicitly in Sec. E. Since the gravitational potential in mass-free regions satisfies Laplace's equation, it follows that if the initial wavepacket is spherically symmetric, there are no quantum corrections to the interferometer phase shift to first order in $V[\mathbf{r}]$. For the numerical values of Table I, we take the initial wavepacket to be twice as large along the interferometer axis than in the transverse dimensions, which gives rise to nonzero quantum corrections at first order in Q_{ijk} . The asymmetry in

the initial wavepacket can be interpreted as arising from asymmetric cooling. For the parameters of Table I, the momentum-space width is smaller along the interferometer axis than in the transverse directions, corresponding to a lower temperature along that axis. In Ref. [75], the authors compute the quantum corrections arising from a first-order expansion of the interferometer phase shift in Q_{ijk} . Using the same choice of initial wavepacket waists, $\beta_1 = \beta_2 = 2\beta_3 = \omega$, our first order result in Q_{ijk} agrees with their first-order expression.

B. Including a Harmonic Component as Part of the Unperturbed Lagrangian

1. Diagram Values

In previous sections we considered treating the harmonic component of the potential (with strength T_{ij}) perturbatively. Consider now a Lagrangian describing a matter wave confined inside of an anharmonic potential with harmonic component (e.g. $\omega_z = \sqrt{T_{zz}}$), and a small cubic component Q_{zzz} , so that the Lagrangian can be described by

$$L_0 = \frac{m}{2} (\dot{x}^2 + \dot{y}^2 + \dot{z}^2) - \frac{m}{2} (\omega_x^2 x^2 + \omega_y^2 y^2 + \omega_z^2 z^2)$$

$$L_1 = -mQ_{zzz}z^3$$

In the case that we absorb the harmonic component of the potential as part of the unperturbed solution, the value of the internal edges of the diagram can be expressed as

$$G_{ab}^{\alpha\alpha}[t_1, t_2] = \frac{1}{2m\hbar} \left(i(\sigma_3)_{ab} \frac{\sin[\omega_\alpha|t_1 - t_2|]}{\omega_\alpha} \right. \\ \left. - (\sigma_2)_{ab} \frac{\sin[\omega_\alpha(t_1 - t_2)]}{\omega_\alpha} \right. \\ \left. + (\sigma_1 - \mathbf{1})_{ab} \left(\frac{\beta_\alpha \sin[\omega_\alpha(t_1 - t_i)] \sin[\omega_\alpha(t_2 - t_i)]}{\omega_\alpha^2} \right. \right. \\ \left. \left. + \frac{\cos[\omega_\alpha(t_1 - t_i)] \cos[\omega_\alpha(t_2 - t_i)]}{\beta_\alpha} \right) \right)$$

where σ_1 , σ_2 , and σ_3 are the Pauli matrices and $\mathbf{1}$ is the identity matrix. Details of this calculation can be found in Sec. A for the 1D rules and and Sec. C for the 3D rules. Note that this value for propagators $G_{ab}^{\alpha\alpha}$ asymptote as $\omega_\alpha \rightarrow 0$ to the propagator value of Sec. III A, where we did not include a harmonic component of the potential in L_0 . The value of the vertex is the same as in Eq. 8 and the value of the external edges $G_a^\alpha[t]$ is as it is defined in Sec. II B, which in this case has a more complicated form than just being proportional to the unperturbed classical trajectory of the arm. Its form depends on the form of the kicks J , and its value is explicitly written out in Sec. A in 1D, and Sec. C in 3D. Consider an interferometer

TABLE I. Phase shift terms for a Mach-Zehnder matter wave interferometer in 3D subject to gravity gradients associated with the spherical nature of the Earth, along with the diagrams which produce the term, ranked in order of the magnitude of their contribution to the total phase shift. The phase shifts are computed with the following parameters: $k_z = 2\pi/(698 \text{ nm})$, $T = 1 \text{ s}$, $g = 9.8 \text{ m/s}^2$, $T_{zz} = -2g/R$, $T_{xx} = T_{yy} = g/R$, $Q_{zzz} = 6g/R^2$, $Q_{xxz} = Q_{yyz} = -3g/R^2$, $S_{zzzz} = -24g/R^3$, $S_{xxxz} = S_{yyzz} = 12g/R^3$, $x_0 = y_0 = z_0 = 0$, $v_z = 3 \text{ m/s}$, $v_x = v_y = 0$, $R = 6.38 \times 10^6 \text{ m}$, $m = 86.91 \text{ u}$, $v_r = \hbar k_z/m$, $\beta_\ell = 2\hbar/(mw_{0,\ell}^2)$ with $\ell = x, y, z$. $w_{0,z} = 2 \text{ mm}$, $w_{0,x} = w_{0,y} = 1 \text{ mm}$. The quantum correction terms are highlighted in light gray.

	Phase Shift	Size [rad]	Diagram
1	$-\frac{m}{\hbar} g v_r T^2$	-8.82×10^7	
2	$\frac{7}{12} \frac{m}{\hbar} g v_r T^4 T_{zz}$	-1.58×10^2	
3	$-\frac{m}{\hbar} v_r v_z T^3 T_{zz}$	8.30×10^1	
4	$-\frac{1}{2} \frac{m}{\hbar} v_r^2 T^3 T_{zz}$	9.10×10^{-2}	
5	$-\frac{31}{120} \frac{m}{\hbar} g^2 v_r T^6 Q_{zzz}$	-3.23×10^{-4}	
6	$\frac{3}{4} \frac{m}{\hbar} g v_r v_z T^5 Q_{zzz}$	2.87×10^{-4}	
7	$-\frac{31}{360} \frac{m}{\hbar} g v_r T^6 T_{zz}^2$	-7.17×10^{-5}	
8	$-\frac{7}{12} \frac{m}{\hbar} v_r v_z^2 T^4 Q_{zzz}$	-6.83×10^{-5}	
9	$\frac{1}{4} \frac{m}{\hbar} v_r v_z T^5 T_{zz}^2$	6.38×10^{-5}	
10	$\frac{3}{8} \frac{m}{\hbar} g v_r^2 T^5 Q_{zzz}$	3.14×10^{-7}	
11	$-\frac{7}{12} \frac{m}{\hbar} v_r^2 v_z T^4 Q_{zzz}$	-1.50×10^{-7}	
12	$\frac{1}{8} \frac{m}{\hbar} v_r^2 T^5 T_{zz}^2$	6.99×10^{-8}	
13	$-\frac{3}{8} \frac{m}{\hbar} g^2 v_r v_z T^7 S_{zzzz}$	8.81×10^{-10}	
14	$\frac{127}{1344} \frac{m}{\hbar} g^3 v_r T^8 S_{zzzz}$	-7.25×10^{-10}	
15	$-\frac{9}{20} \frac{m}{\hbar} g v_r v_z T^7 Q_{zzz} T_{zz}$	5.29×10^{-10}	
16	$\frac{127}{1120} \frac{m}{\hbar} g^2 v_r T^8 Q_{zzz} T_{zz}$	-4.35×10^{-10}	
17	$\frac{31}{60} \frac{m}{\hbar} g v_r v_z^2 T^6 S_{zzzz}$	-3.72×10^{-10}	
18	$\frac{31}{72} \frac{m}{\hbar} v_r v_z^2 T^6 Q_{zzz} T_{zz}$	-1.55×10^{-10}	
19	$-\frac{1}{6} \frac{m}{\hbar} v_r^3 T^4 Q_{zzz}$	-9.38×10^{-11}	
20	$-\frac{1}{4} \frac{m}{\hbar} v_r v_z^3 T^5 S_{zzzz}$	5.50×10^{-11}	
21	$-\frac{1}{40} \frac{m}{\hbar} v_r v_z T^7 T_{zz}^3$	1.96×10^{-11}	
22	$\frac{127}{20160} \frac{m}{\hbar} g v_r T^8 T_{zz}^3$	-1.61×10^{-11}	
23	$-\frac{1}{4} \frac{1}{\beta_z} v_r T^2 Q_{zzz}$	-6.50×10^{-12}	
24	$-\frac{3}{16} \frac{m}{\hbar} g^2 v_r^2 T^7 S_{zzzz}$	9.66×10^{-13}	
25	$\frac{31}{60} \frac{m}{\hbar} g v_r^2 v_z T^6 S_{zzzz}$	-8.15×10^{-13}	
26	$-\frac{1}{4} \frac{1}{\beta_x} v_r T^2 Q_{xxz}$	8.13×10^{-13}	
27	$-\frac{1}{4} \frac{1}{\beta_y} v_r T^2 Q_{yyz}$	8.13×10^{-13}	
28	$-\frac{9}{40} \frac{m}{\hbar} g v_r^2 T^7 Q_{zzz} T_{zz}$	5.80×10^{-13}	
29	$\frac{31}{72} \frac{m}{\hbar} v_r^2 v_z T^6 Q_{zzz} T_{zz}$	-3.40×10^{-13}	
30	$-\frac{3}{8} \frac{m}{\hbar} v_r^2 v_z^2 T^5 S_{zzzz}$	1.81×10^{-13}	

sequence where the two arms are kicked symmetrically, and the external force on the two arms which emerge in the same output port is expressed by

$$\frac{J_a^3[t]}{m v_r} = \begin{cases} 2\delta[t-0] - 4\delta[t-T] + 2\delta[t-2T] & a = 1 \\ -2\delta[t-0] + 4\delta[t-T] - 2\delta[t-2T] & a = 2 \end{cases} \quad (12)$$

Here one arm of the interferometer ($a = 1$) is kicked with 2 recoils ‘upward’ at time $t = 0$, 4 recoils ‘downward’ at time $t = T$, and 2 recoils ‘upward’ at time $t = 2T$. The other arm ($a = 2$) is kicked with equal and opposite recoils to the first. We take the interferometer beam to be oriented perfectly along the z axis so that no component of the laser recoils are directed in the transverse dimensions, $J_a^1[t] = J_a^2[t] = 0$. We take the initial center-of-mass (COM) position and velocity of the Gaussian wavepacket to be zero. In this case, under only a harmonic potential, the phase shift would be zero owing to the mirror symmetry of the potential and the symmetry with which the two arms of the interferometer are kicked. The small cubic non-linearity in L_1 breaks that mirror symmetry and produces a non zero phase shift.

There is a way in which the semi-classical approach to computing phase shifts breaks down. It is the case that the phase shift of an interferometer does not change after the final beamsplitter. In the semi-classical formalism, and in the absence of a cubic nonlinearity, this property is satisfied by the fact that the additional accumulated separation phase between two the arms which compose a single output port exactly cancels with the additionally accumulated propagation phase after the final beamsplitter. Under a cubic nonlinearity, however, the propagation and separation phases accumulated after the final beamsplitter no longer cancel, and what results is a computed phase shift which changes as a function of the time after the final beamsplitter. In the diagrammatic approach, on the other hand, the phase shift is correctly predicted to be independent of the time after the final beamsplitter pulse.

2. Validating with Numerics in 1D

To demonstrate agreement with evaluating the phase shift numerically, as in Sec. III A 2, we evaluate phase shifts in a parameter space where quantum corrections are heightened beyond physical realism (parameters indicated in caption of Fig. 3). Fig. 3 compares the result of evaluating these phase shifts numerically (black dots), via the semi-classical formalism (dashed gray line), and via the diagrammatic formalism (solid gray line). The semi-classical solution is plotted evaluating the phase shift at the time immediately following the final beamsplitter, even though technically its value changes as a function of time after the final beamsplitter as discussed earlier. The two three-vertex diagrams which contribute to the phase shift are included in an inset of panel (a). Panel (b) indicates the semi classical trajectories of the two interferometer arms (black lines), along with the wavepacket size (blue for the upper arm and red for the lower). Panel (c) plots the shape of the potential, which is anharmonic owing to a small cubic dependence which breaks the mirror symmetry of the system about $z = 0$.

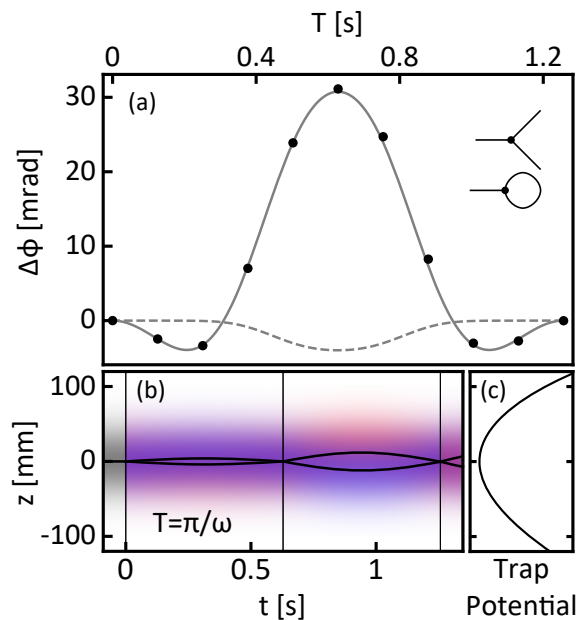


FIG. 3. Simulation of matter wave interferometer confined to an anharmonic trap in 1D. Simulation parameters (in SI units) are $\hbar/m = 10^{-2}$, $w_{0,z} = 0.0632456$, $\omega = 5$, $v_z = 0$, $v_r = 10^{-2}$, $Q_{zzz} = 10^2$, $\Delta z = 5 \times 10^{-4}$, $\Delta t = 5 \times 10^{-4}$. The waist $w_{0,z}$ is chosen so that the initial wavepacket is the ground state of the harmonic potential. (a) Numerically computed phase shifts (black dots), along with the semi-classically computed phase (dashed gray line) and diagrammatically computed phase (solid gray line). The two diagrams that contribute to the leading order phase shift in Q_{zzz} are displayed on the right hand side. (b) Classical trajectories of the two interferometer arms (solid black lines) along with the width of the wavepackets associated with both interferometer arms (blue and red). The trajectories are plotted for the interrogation time for which the phase shift is maximized ($T = \pi/\omega$). (c) The form of the anharmonic trapping potential, to contextualize the classical trajectories.

3. 3D Calculation of Phase Shifts in Matter Wave Interferometers Confined in Anharmonic Traps

Here we apply the analytic expressions which emerge from the diagrammatic formalism to an experimentally realistic case of a matter wave confined to a magnetic trap [107]. Following the experimental parameters of a time-orbiting potential magnetic trap used for Bose-Einstein condensate atom interferometry with ^{87}Rb [108], we consider a trap frequency of $\omega = 2\pi \times 11.2$ Hz, a trap anharmonicity of $Q_{zzz} = 9.98 \times 10^6 \text{m}^{-2}\text{s}^{-1}$, no initial COM velocity, a recoil velocity of $v_r \approx 5.89$ mm/s, and an initial wavepacket waist of $w_0 = 10\mu\text{m}$ [109]. The value of w_0 comes from the observed condensate size in [110]. Figure 4 shows expected phase shifts under a sequence where the two arms are kicked symmetrically. In this scenario, the quantum corrections are on the order of the semi-classically computed phase shifts. The leading-order quantum corrections are approximately 1 mrad and

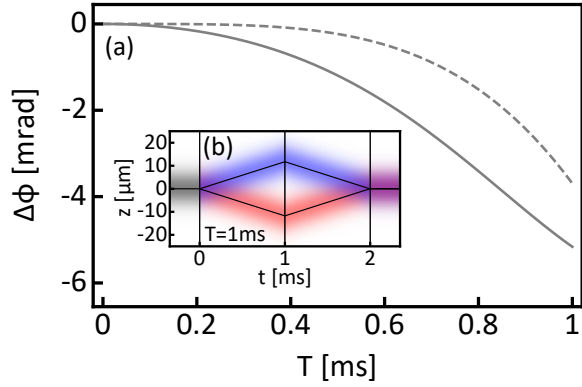


FIG. 4. (a) Quantum corrections for a trapped matter wave interferometer with experimentally realistic parameters, computed via the semi-classical method (dashed gray line) and the diagrammatic method (solid gray line). In the semi-classical computation, the phase shift is evaluated immediately after the final beamsplitter. (b) The corresponding interferometer arms for a 1 ms interrogation time interferometer sequence. The black lines indicate the classical trajectories and the blue and red density plots indicate the wavepacket waist of the two interferometer arms. The computed interferometer contrast drops to $\approx 73\%$ at $T = 1$ ms owing to the two arms of the interferometer imperfectly overlapping at the time of the final beamsplitter.

might therefore be observable. This example suggests that beyond-semi-classical corrections to the interferometer phase could be important to consider for accurately modeling trapped interferometers.

The numerical value of the condensate size used in this calculation is larger than the harmonic oscillator ground state size, possibly due to repulsive mean-field interactions in the BEC. The diagrammatic calculator does not include interaction effects, which can be important for accurate phase shift predictions in this regime [111]. In addition, when we refer to the initial ground state wavefunction size, we neglect the anharmonic corrections to the true ground state of the trap and treat the initial wavepacket as Gaussian. We assume the non-Gaussian features of the wavepacket prior to the first beamsplitter pulses are small compared to those generated during free propagation in the interferometer sequence. Both interaction effects and non-Gaussian initial-state corrections from trap anharmonicities may contribute additional phase shift contributions that are not captured in the present calculation.

IV. APPLICATION: PHASE SHIFT FOR POTENTIALS WITH ARBITRARY SPATIAL DEPENDENCE

In this section, we will consider external potential with more complicated dependence on z . We will use the diagrammatic formalism outlined in Sec. II B to compute phase shifts to all orders in z , but only first order in ϵ by

summing over all 1-vertex diagrams.

A. Calculation of Phase Shift by Summing Over All 1-Vertex Diagrams in 1D

Consider the Lagrangian

$$L_1 = -m\phi_g[z]$$

where ϕ_g is a gravitational potential with an arbitrary spatial dependence. We will write out the value of a diagram with an arbitrary number of external edges and loops, then sum over the number of external edges and loops. This will amount to summing over the potentially infinite number of one vertex diagrams associated with the potentially infinite number of Taylor series coefficients in the potential $\phi_g[z] = \sum_{n=0}^{\infty} \frac{1}{n!} c_n z^n$. A diagram with j external edges and k loops will have value $\mathcal{A}[j, k]$, where

$$\mathcal{A}[j, k] =$$

We can write the value of this diagram in terms of the symmetry factor, vertex value, and edge values as $\mathcal{A}[j, k] = (SYM)(VERT)(EDGE)$ with

$$SYM = \frac{1}{j!k!2^k}$$

$$VERT = (-m)\lambda_a^{j+2k} \int_{t_i}^{t_f} dt$$

$$EDGE = (G_a^3[t])^j (G_{aa}^{33}[t, t])^k$$

Using Eq. 8, we can write this value as $\mathcal{A}[j, k] = \mathcal{A}_1[j, k] + \mathcal{A}_2[j, k]$ where we explicitly write out the summation over the Latin index a , and

$$\begin{aligned} \mathcal{A}_a[j, k] = & \frac{1}{j!k!2^k} \left((-1)^{a+1} \frac{\hbar}{i} \right)^{j+2k-1} (-m\epsilon) c_{j+2k} \\ & \times \int_{t_i}^{t_f} dt (G_a^3[t])^j (G_{aa}^{33}[t, t])^k \end{aligned} \quad (13)$$

with $a = 1, 2$. We can solve for the phase shift by summing over the number of external edges and loops. If we express the phase shift as a Taylor series in ϵ , $\Delta\phi = \Delta\phi^{(0)} + \Delta\phi^{(1)}\epsilon + \mathcal{O}[\epsilon^2]$, then

$$\Delta\phi^{(1)} = \text{Im} \left[\sum_{a=1}^2 \sum_{j=0}^{\infty} \sum_{k=0}^{\infty} \mathcal{A}_a[j, k] \right]$$

We start by evaluating the sum over the number of external edges j

$$\begin{aligned} \sum_{j=0}^{\infty} \mathcal{A}_a[j, k] &= -m\epsilon \int_{t_i}^{t_f} dt \frac{1}{k!2^k} \left((-1)^{a+1} \frac{\hbar}{i} \right)^{2k-1} (G_{aa}^{33}[t, t])^k \\ &\quad \times \sum_{j=0}^{\infty} \frac{1}{j!} c_{j+2k} \left((-1)^{a+1} \frac{\hbar}{i} G_a^3[t] \right)^j \\ &= -m\epsilon \int_{t_i}^{t_f} dt \frac{1}{k!2^k} \left((-1)^{a+1} \frac{\hbar}{i} \right)^{2k-1} (G_{aa}^{33}[t, t])^k \\ &\quad \times \partial_z^{2k} \phi_g[z] \Big|_{z=(-1)^{a+1} \frac{\hbar}{i} G_a^3[t]} \end{aligned} \quad (14)$$

where to arrive at the second equality, we applied the identity $\sum_{j=0}^{\infty} \frac{1}{j!} c_{j+2k} z^j = \partial_z^{2k} \sum_{j=0}^{\infty} \frac{1}{j!} c_j z^j = \partial_z^{2k} \phi_g[z]$. Now performing the sum over the number of loops k , we have

$$\begin{aligned} \sum_{k=0}^{\infty} \sum_{j=0}^{\infty} \mathcal{A}_a[j, k] &= -m\epsilon \left((-1)^{a+1} \frac{\hbar}{i} \right)^{-1} \int_{t_i}^{t_f} dt \\ &\quad \times \sum_{k=0}^{\infty} \frac{1}{k!} \left(-\frac{1}{2} \hbar^2 G_{aa}^{33}[t, t] \partial_z^2 \right)^k \phi_g[z] \Big|_{z=(-1)^{a+1} \frac{\hbar}{i} G_a^3[t]} \\ &= -m\epsilon (-1)^{a+1} \frac{i}{\hbar} \int_{t_i}^{t_f} dt \\ &\quad \times e^{-\frac{1}{2} \hbar^2 G_{aa}^{33}[t, t] \partial_z^2} \phi_g[z] \Big|_{z=(-1)^{a+1} \frac{\hbar}{i} G_a^3[t]} \\ &= (-1)^{a+1} \frac{-im\epsilon}{\hbar} \int_{t_i}^{t_f} dt \bar{\phi}_g \left[i\hbar (-1)^a G_a^3[t], t \right] \end{aligned}$$

with

$$\bar{\phi}_g[z, t] = \int_{-\infty}^{\infty} dz' \left(\frac{1}{-2\pi\hbar^2 G_{aa}^{33}[t, t]} \right)^{1/2} \times e^{\frac{1}{2\hbar^2 G_{aa}^{33}[t, t]} (z-z')^2} \phi_g[z']$$

where to arrive at the third equality, we used the identity [112]

$$e^{b\partial_x^2} \phi_g[x] = \int_{-\infty}^{\infty} dx' \left(\frac{1}{4\pi b} \right)^{1/2} e^{-\frac{1}{4b}(x-x')^2} \phi_g[x']$$

where $b > 0$. This expression is valid whether we include a harmonic component as part of the unperturbed potential or not. If we choose not to include a harmonic component as part of the unperturbed potential, such that

$$L_0 = \frac{m}{2} \dot{z}^2 - mgz$$

then referencing the propagators of Sec. III A, we have

$$G_{11}^{33}[t, t] = G_{22}^{33}[t, t] = -\frac{1}{2m\hbar} \left(\beta_3 t^2 + \frac{1}{\beta_3} \right)$$

and referencing the external edge values of Eq. 11, the first order correction to the phase shift can be written out as

$$\Delta\phi^{(1)} = -\frac{m}{\hbar} \int_{t_i}^{t_f} dt \left(\bar{\phi}_g[z_{cl,1}^{(0)}[t], t] - \bar{\phi}_g[z_{cl,2}^{(0)}[t], t] \right) \quad (15)$$

where

$$\begin{aligned} \bar{\phi}_g[z, t] &= \int_{-\infty}^{\infty} dz' \left(\frac{1}{\pi(\hbar/m)(\beta_3 t^2 + 1/\beta_3)} \right)^{1/2} \\ &\quad \times e^{-\frac{1}{(\hbar/m)(\beta_3 t^2 + 1/\beta_3)} (z-z')^2} \phi_g[z'] \end{aligned}$$

Each one-vertex diagram has pure imaginary value, resulting in no corrections to the contrast at first order in the potential ϕ_g . For comparison, following the usual semi-classical formalism, the correction to the phase shift to first order in the potential can be written as [65]

$$\Delta\phi^{(1)} = -\frac{m}{\hbar} \int_{t_i}^{t_f} dt \left(\phi_g[z_{cl,1}^{(0)}[t]] - \phi_g[z_{cl,2}^{(0)}[t]] \right) \quad (16)$$

if the unperturbed classical trajectories have the same position and velocity at the time of the final beamsplitter. In Sec. IV B, we use Eq. 15 to compute higher order quantum corrections to matter wave interferometers under more interesting spatially dependent potentials, and compare to the results of a numerical simulation in 1D.

The 3D extension of Eq. (15) is derived in detail in the supplement (Sec. E), but is conceptually similar to the 1D result. Instead of defining $\bar{\phi}_g$ as a convolution in z between a gaussian function and the classical potential ϕ_g , the convolution is now carried out over all three Cartesian dimensions of the system. As described in Sec. III A 3, even if the semi-classical trajectories that correspond to the atom wavepacket remain along the z -axis, quantum corrections can still depend on the gravitational field strength in transverse directions. Therefore, when performing calculations or making estimates with realistic physical parameters (rather than the simplified parameters used for 1D simulations) it can be important to work with the fully 3D expressions.

B. Agreement With Numerics in 1D

Here we validate Eq. 15 by numerically solving for the phase response of a matter wave interferometer to the gravitational potential from a proof mass. We use nonphysical simulation parameters to amplify quantum

corrections, as done in Sections III A 2, and III B 2. In Sec. IV C, we estimate the phase response using realistic experimental parameters.

Consider a system where the gravitational potential $\phi_g[z]$ emerges from a 1D ring shaped proof mass with radius R and total mass M aligned with the interferometer axis z , along with a linear gravity term from the Earth, such that the potential contributed by the proof mass has the form

$$\phi_g[z] = -\frac{GM}{\sqrt{R^2 + z^2}} \quad (17)$$

where G is Newton's gravitational constant, and the unperturbed Lagrangian does not have the harmonic component included, $L_0 = m\dot{z}^2/2 - mgz$. This potential has an infinite number of Taylor series coefficients in z , so computing phase shifts perturbatively in z could lead to inaccurate predictions. In Fig. 5, we display the result of computing the phase shift in an unphysical parameter space where quantum corrections are heightened (see caption for simulation parameters). Panel (a) contains the phase shift as determined by a split step wavepacket simulation (black dots), the semi-classical method (gray dashed line) and the diagrammatic method (gray solid line). The semi-classical phase shift is determined by numerically evaluating the integral over time of Eq. 16, and the diagrammatic phase shift calculation is performed by numerically evaluating the integrals over space and time of Eq. 15. The inset of that panel indicates the summation that is performed to arrive at the diagrammatically evaluated phase shift. Here we plot the first order correction in ϵ , which in this case is also the first order correction in Newton's gravitational constant G . $\Delta\phi = \Delta\phi^{(0)} + \Delta\phi^{(1)}G + \mathcal{O}[G^2]$, where $\Delta\phi^{(0)} = -\frac{m}{\hbar}v_r g T^2$. The Mach-Zehnder pulse sequence simulated here corresponds to a source term J_a that has the same form as that of Eq. 10.

The 'smearing' effect on the phase response of the interferometer, resulting from incorporating the finite size of the matter wavepacket into the phase shift calculation, suppresses the peak response from the semi-classically computed phase. This suppression highlights how higher order quantum corrections could manifest as sources of systematic error. Panel (b) presents the semi-classical trajectories (black lines) associated with the two interferometer arms in this parameter space for $T = 0.5$ s. The density plot indicates the finite extent of the wavepackets of the two interferometer arms (blue and red). Panel (c) shows the shape of the external potential $\phi_g[z]$ in relation to the classical trajectories and the size of the wavepackets.

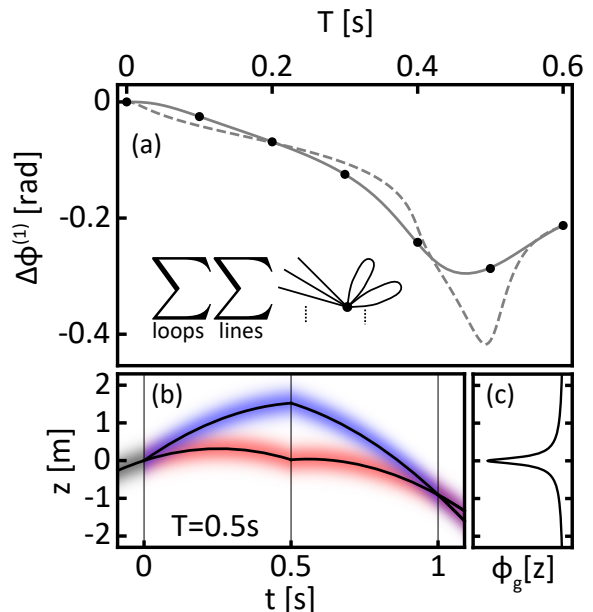


FIG. 5. Simulation of phase shift from proof mass potential. (a) The numerically evaluated interferometer phase as a function of the interrogation time T (black points), superimposed with the phase shifts as computed via the semi-classical method (dashed gray line, Eq. 16) and the diagrammatic method (solid gray line, Eq. 15). The diagrammatic solution comes from evaluating the sum over an infinite number of 1-vertex diagrams, as indicated by the expression in the left hand side. (b) The two arms of the interferometer for a $T = 0.5$ s sequence. The black lines denote the classical trajectories and the red and blue density plots denote the wavepackets associated with the two interferometer arms. (c) The form of the proof mass potential (Eq. 17), for reference against the arm trajectories. The calculations are performed using the following parameters (in SI units): $w_0 = 0.5$, $\hbar/m = 10^{-2}$, $v_z = 2.5$, $v_r = 3$, $g = 10$, $GM = 10^{-3}$, $R = 7 \times 10^{-2}$, $\Delta z = 1.25 \times 10^{-3}$, $\Delta t = 2.5 \times 10^{-4}$.

C. 3D Calculation of Response of Matter Wave Interferometer to Proof-Mass Potential

Here we estimate the scale of quantum corrections in a 3D system under realistic experimental parameters associated with the response of an interferometer in the presence of a gravitational potential from a proof mass. We consider a proof mass with nonzero 3D thickness, rather than the 1D ring proof mass of Sec. IV B. Computing higher-order quantum corrections to proof mass potentials using the 3D version of Eq. 15 (see Eq. (E2)) can be challenging in a physical parameter space because the Gaussian over which proof mass potential is convolved can be narrow relative to the span of the potential along the interferometer axis. For instance, referencing the 1D calculation Eq. (15) with $w_{0,z} = 10 \mu\text{m}$, $t = 2.8$ s, and $\hbar/m = 7.25 \times 10^{-10} \text{ m}^2/\text{s}$, the standard deviation of the Gaussian is $\sigma = \frac{1}{2} \sqrt{(w_{0,z})^2 + \frac{4\hbar^2 t^2}{m^2 (w_{0,z})^2}} \approx 0.2 \text{ mm}$, which is small compared to meter-scale span of the proof

mass potential. The semi-classical approximation takes the limit that the Gaussian over which the potential is convolved is a delta function (see Equations 15 and 16). Quantum corrections are encoded in the small but finite width of this Gaussian. It is computationally expensive to reliably evaluate quantum corrections by numerically evaluating the convolution integral owing to the large grid sampling required by the large span of the proof mass potential, and the fine grid resolution required by the narrow Gaussian. A more productive approach is to evaluate Eq. 15 analytically order by order in σ , then integrate each term numerically in time. This approach is akin to using Eq. (14) to evaluate the corrections, where $k = 0$ corresponds to the semi-classical case, and $k \geq 1$ terms contain the quantum corrections. In this parameter space, the contributions for larger values of k , which encode higher-order quantum corrections, decrease as k increases. The extension of these ideas to 3D are worked out in detail in Sec. F. In Fig. 6, the quantum correction to the interferometer phase shift is displayed as a function of the size of the initial wavepacket waist along the interferometer axis $w_{0,z}$, along with the associated atom cloud temperature along that axis, and a cartoon of the proof mass dimensions used to generate the potential. The vertical vacuum tube, whose axis of cylindrical symmetry is co-linear with the interferometer axis (the z axis), has a 15 cm outer diameter. The proof mass is a hollow cylinder with the density of Tungsten, an inner radius of 0.1 m, an external radius of 0.5 m, and a height of 0.2 m. The quantum corrections to the phase shift, $\Delta\phi_{\text{qu}}$, are computed by evaluating the terms in the 3D version of Eq. 14 (Eq. (F4)) by taking derivatives of the analytic form of the thick proof mass potential and integrating numerically in time (see Sec. F for details). For certain values of $w_{0,z}$, the scale of these quantum corrections can be $> \text{mrad}$, which could be measurable. This result indicates that quantum corrections to the phase shift might need to be considered for gravitational experiments with proof masses, including precision measurements of Newton's gravitational constant G or searches for fifth forces.

D. Conditions for Quantum Corrections to Vanish to First Order in External Potential

If the initial wavepacket has equal waists in all directions (i.e. it is prepared with spherical symmetry), such that $w_{0,x} = w_{0,y} = w_{0,z}$, then we have $\beta_1 = \beta_2 = \beta_3 = \beta$ and $G_{aa}^{\alpha\alpha}[t, t]$ becomes independent of the Latin and Greek indices

$$G_{aa}^{\alpha\alpha}[t, t] = -\frac{1}{2m\hbar} \left(\beta t^2 + \frac{1}{\beta} \right) \quad \forall \alpha = 1, 2, 3, a = 1, 2$$

Under these conditions, the value of $\Delta\phi^{(1)}$ expressed in 3D can be written as

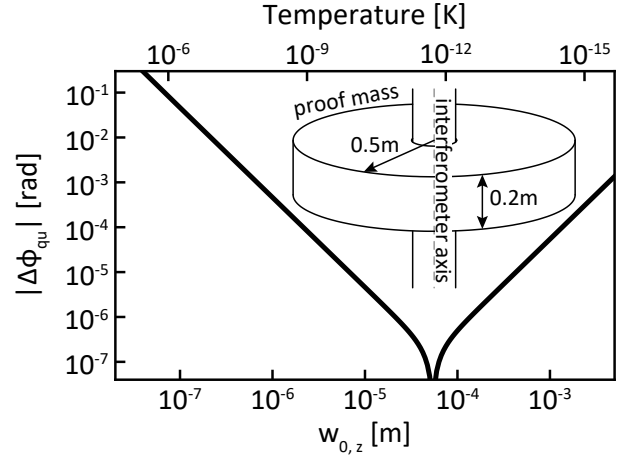


FIG. 6. Estimate of quantum corrections to interferometer phase shift to first order in the proof mass potential for a ≈ 2933 kg proof mass. It is assumed that the interferometer has a 100 photon recoil momentum splitting, $T \approx 1.40$ s, and $v_z \approx 13.35$ m/s. We take the interferometer to operate on the 698 nm clock transition of ^{87}Sr . The first order semi-classical contribution from just the proof masses is ≈ 240 rad. As we scan the longitudinal initial wavepacket waist $w_{0,z}$, we keep the initial transverse waist sizes fixed relative to it by setting $w_{0,x} = w_{0,y} = w_{0,z}/\sqrt{2}$. The temperature is defined relative to the z -axis. The relationship between temperature and beam waist is taken to be $w_{0,z} = \hbar/\sqrt{mk_B T_K}$, where m is the mass of the strontium atom, k_B is Boltzmann's constant and T_K is the effective temperature. A 0.15 m outer diameter vacuum tube is indicated for reference. The inner diameter of the proof mass is 0.2m and the position of the center of the proof mass is 0.2 m below the apex of the upper interferometer arm's trajectory along the interferometer axis. The axis of the interferometer, z , is indicated in the dashed gray line.

$$\Delta\phi^{(1)} = \frac{m}{\hbar} \int_{t_i}^{t_f} dt \sum_{a=1}^2 (-1)^a \left(e^{-\frac{\hbar^2}{2} G_{aa}^{\alpha\alpha}[t, t] \nabla^2} \phi_g[r_1, r_2, r_3] \right) \Big|_{r_\ell = r_{\text{cl}, a}^\ell[t]} \quad (18)$$

where $r_1 = x$, $r_2 = y$, $r_3 = z$ and

$$r_{\text{cl}, a}^\ell[t] = \begin{cases} x_{\text{cl}, a}^{(0)}[t], & \ell = 1 \\ y_{\text{cl}, a}^{(0)}[t], & \ell = 2 \\ z_{\text{cl}, a}^{(0)}[t], & \ell = 3 \end{cases}$$

This result is computed in greater detail in Sec. E. Taylor expanding the exponential in the integrand of Eq. (18). The zeroth order expansion reproduces the semi-classical result the n^{th} order expansion has the factor $\nabla^{2n} \phi_g$ in the integrand. If ϕ_g satisfies Laplace's equation $\nabla^2 \phi_g = 0$, then $\nabla^{2n} \phi_g = 0 \quad \forall n \geq 1$, and all quantum corrections to $\Delta\phi^{(1)}$ vanish. In summary, if the initial

atom wavefunction is spherically symmetric, and the external potential ϕ_g satisfies Laplace's equation, then the first order correction to the interferometer phase shift in ϕ_g will have no quantum corrections.

V. OUTLOOK

We have introduced a new formalism for analytically calculating quantum corrections to the traditional semiclassical approximations used to analyze matter wave interferometers. We have applied this formalism to examples involving anharmonic traps and gravitational potentials from a local proof mass, and demonstrated that these quantum corrections can be significant for realistic experimental parameters. It could therefore be important to consider and account for their effects in future measurements.

In future work, it could be productive to investigate the application of this approach to rotating frames of reference, in which Coriolis forces emerge, leading to terms in the Lagrangian that couple position and momentum operators. The generalization of the calculation to non-Gaussian initial wavepackets is another direction for future study. Corrections to the interferometer phase that are higher than first order in an external potential with arbitrary spatial dependence can also be evaluated by summing over the infinite number of 2-vertex diagrams in the same manner as was done in Sec. IV C. In this case, the two-vertex diagrams can be parametrized in by five parameters: the number of external edges and loops on one vertex, the number of external edges and loops on the other, and the number of internal edges between them. Then a sum can be performed over the five parameters to arrive at an analytic expression for the phase shift at second order in the arbitrary potential. The diagrammatic framework could also be extended to include phase shift corrections arising from multipath interference [113], such as those appearing in trapped, multi-loop interferometer gyroscopes [89, 90], rather than just the simpler two-arm configurations considered in this paper. In addition to computing interferometer phase shifts, this formalism could also be applied to computing perturbative corrections to matter

wavepackets themselves as they evolve in anharmonic potentials. Furthermore, owing to the structural similarity of the free particle Schrodinger equation and the paraxial wave equation, this formalism could prove useful for generating analytic expressions for the profiles of Gaussian laser beams propagating with small aberrations.

ACKNOWLEDGMENTS

We dedicate this paper to Ernst Maria Rasel in celebration of his 60th birthday. His groundbreaking work to broadly push the boundaries of atom interferometry, through advances such as pioneering atom interferometry in microgravity and inventing many new atom optics techniques, is a constant source of inspiration. We thank Cass Sackett and Michael Kagan for valuable discussions. This work was produced by Fermi Forward Discovery Group, LLC under Contract No. 89243024CSC000002 with the U.S. Department of Energy, Office of Science, Office of High Energy Physics. The United States Government retains and the publisher, by accepting the work for publication, acknowledges that the United States Government retains a non-exclusive, paid-up, irrevocable, world-wide license to publish or reproduce the published form of this work, or allow others to do so, for United States Government purposes. The Department of Energy will provide public access to these results of federally sponsored research in accordance with the DOE Public Access Plan (<http://energy.gov/downloads/oe-public-access-plan>). This material is based upon work supported by the U.S. Department of Energy, Office of Science, National Quantum Information Science Research Centers, Superconducting Quantum Materials and Systems Center (SQMS) under contract number DE-AC02-07CH11359. This work is funded in part by the Gordon and Betty Moore Foundation (Grant GBMF7945), the David and Lucile Packard Foundation (Fellowship for Science and Engineering), and the Office of Naval Research (Grant Number N00014-19-1-2181). JG acknowledges support from a National Science Foundation (NSF) Quantum Information Science and Engineering Network (QISE-NET) Graduate Fellowship, funded by NSF award No. DMR-1747426.

-
- [1] A. D. Cronin, J. Schmiedmayer, and D. E. Pritchard, Optics and interferometry with atoms and molecules, *Rev. Mod. Phys.* **81**, 1051 (2009).
 - [2] A. Peters, K. Y. Chung, and S. Chu, High-precision gravity measurements using atom interferometry, *Metrologia* **38**, 25 (2001).
 - [3] J. M. McGuirk, G. T. Foster, J. B. Fixler, M. J. Snadden, and M. A. Kasevich, Sensitive absolute-gravity gradiometry using atom interferometry, *Phys. Rev. A* **65**, 033608 (2002).
 - [4] D. S. Durfee, Y. K. Shaham, and M. A. Kasevich, Long-term stability of an area-reversible atom-interferometer sagnac gyroscope, *Phys. Rev. Lett.* **97**, 240801 (2006).
 - [5] X. Wu, Z. Pagel, B. S. Malek, T. H. Nguyen, F. Zi, D. S. Scheirer, and H. Müller, Gravity surveys using a mobile atom interferometer, *Sci. Adv.* **5**, eaax0800 (2019).
 - [6] K. Bongs, M. Holynski, J. Vovrosh, P. Bouyer, G. Condon, E. Rasel, C. Schubert, W. P. Schleich, and A. Roura, Taking atom interferometric quantum sensors from the laboratory to real-world applications, *Nat. Rev. Phys.* **1**, 731 (2019).

- [7] Y. Bidel, N. Zahzam, A. Bresson, C. Blanchard, M. Cadoret, A. V. Olesen, and R. Forsberg, Absolute airborne gravimetry with a cold atom sensor, *Journal of Geodesy* **94**, 20 (2020).
- [8] B. Canuel, A. Bertoldi, L. Amand, E. Pozzo di Borgo, T. Chantrait, C. Danquigny, M. Dovale Álvarez, B. Fang, A. Freise, R. Geiger, J. Gillot, S. Henry, J. Hinderer, D. Holleville, J. Junca, G. Lefèvre, M. Merzougui, N. Mielec, T. Monfret, S. Pelisson, M. Prevedelli, S. Reynaud, I. Riou, Y. Rogister, S. Rosat, E. Cormier, A. Landragin, W. Chaibi, S. Gaffet, and P. Bouyer, Exploring gravity with the miga large scale atom interferometer, *Scientific Reports* **8**, 14064 (2018).
- [9] K. Bongs, R. Launay, and M. A. Kasevich, High-order inertial phase shifts for time-domain atom interferometers, *Applied Physics B* **84**, 599 (2006).
- [10] J. K. Stockton, K. Takase, and M. A. Kasevich, Absolute geodetic rotation measurement using atom interferometry, *Phys. Rev. Lett.* **107**, 133001 (2011).
- [11] G. W. Biedermann, X. Wu, L. Deslauriers, S. Roy, C. Mahadeswaraswamy, and M. A. Kasevich, Testing gravity with cold-atom interferometers, *Phys. Rev. A* **91**, 033629 (2015).
- [12] S. Fray, C. A. Diez, T. W. Hänsch, and M. Weitz, Atomic interferometer with amplitude gratings of light and its applications to atom based tests of the equivalence principle, *Phys. Rev. Lett.* **93**, 240404 (2004).
- [13] D. Schlippert, J. Hartwig, H. Albers, L. L. Richardson, C. Schubert, A. Roura, W. P. Schleich, W. Ertmer, and E. M. Rasel, Quantum test of the universality of free fall, *Phys. Rev. Lett.* **112**, 203002 (2014).
- [14] L. Zhou, S. Long, B. Tang, X. Chen, F. Gao, W. Peng, W. Duan, J. Zhong, Z. Xiong, J. Wang, Y. Zhang, and M. Zhan, Test of equivalence principle at 10^{-8} level by a dual-species double-diffraction raman atom interferometer, *Phys. Rev. Lett.* **115**, 013004 (2015).
- [15] C. C. N. Kuhn, G. D. McDonald, K. S. Hardman, S. Bennetts, P. J. Everitt, P. A. Altin, J. E. Debs, J. D. Close, and N. P. Robins, A bose-condensed, simultaneous dual-species mach-zehnder atom interferometer, *New Journal of Physics* **16**, 073035 (2014).
- [16] M. G. Tarallo, T. Mazzoni, N. Poli, D. V. Sutyryn, X. Zhang, and G. M. Tino, Test of einstein equivalence principle for 0-spin and half-integer-spin atoms: Search for spin-gravity coupling effects, *Phys. Rev. Lett.* **113**, 023005 (2014).
- [17] A. Bonnin, N. Zahzam, Y. Bidel, and A. Bresson, Simultaneous dual-species matter-wave accelerometer, *Phys. Rev. A* **88**, 043615 (2013).
- [18] J. Hartwig, S. Abend, C. Schubert, D. Schlippert, H. Ahlers, K. Posso-Trujillo, N. Gaaloul, W. Ertmer, and E. M. Rasel, Testing the universality of free fall with rubidium and ytterbium in a very large baseline atom interferometer, *New Journal of Physics* **17**, 035011 (2015).
- [19] P. Asenbaum, C. Overstreet, M. Kim, J. Curti, and M. A. Kasevich, Atom-interferometric test of the equivalence principle at the 10^{-12} level, *Phys. Rev. Lett.* **125**, 191101 (2020).
- [20] J. Williams, S. wey Chiow, N. Yu, and H. Müller, Quantum test of the equivalence principle and space-time aboard the international space station, *New Journal of Physics* **18**, 025018 (2016).
- [21] B. Battelier, J. Bergé, A. Bertoldi, L. Blanchet, K. Bongs, P. Bouyer, C. Braxmaier, D. Calonico, P. Fayet, N. Gaaloul, C. Guerlin, A. Hees, P. Jetzer, C. Lämmerzahl, S. Lecomte, C. Le Poncin-Lafitte, S. Loriani, G. Métris, M. Nofrarias, E. Rasel, S. Reynaud, M. Rodrigues, M. Rothacher, A. Roura, C. Salomon, S. Schiller, W. P. Schleich, C. Schubert, C. F. Sopuerta, F. Sorrentino, T. J. Sumner, G. M. Tino, P. Tuckey, W. v. Klitzing, L. Wörner, P. Wolf, and M. Zelan, Exploring the foundations of the physical universe with space tests of the equivalence principle, *Experimental Astronomy* **51**, 1695–1736 (2021).
- [22] G. Rosi, G. D’Amico, L. Cacciapuoti, F. Sorrentino, M. Prevedelli, M. Zych, Č. Brukner, and G. M. Tino, Quantum test of the equivalence principle for atoms in coherent superposition of internal energy states, *Nature Communications* **8**, 15529 (2017).
- [23] B. Barrett, L. Antoni-Micollier, L. Chichet, B. Battelier, T. Lévêque, A. Landragin, and P. Bouyer, Dual matter-wave inertial sensors in weightlessness, *Nature Communications* **7**, 13786 (2016).
- [24] J. G. Wacker, Using atom interferometry to search for new forces, *Physics Letters B* **690**, 38 (2010).
- [25] J. B. Fixler, G. T. Foster, J. M. McGuirk, and M. A. Kasevich, Atom interferometer measurement of the newtonian constant of gravity, *Science* **315**, 74 (2007), <https://www.science.org/doi/pdf/10.1126/science.1135459>.
- [26] G. Rosi, F. Sorrentino, L. Cacciapuoti, M. Prevedelli, and G. M. Tino, Precision measurement of the newtonian gravitational constant using cold atoms, *Nature* **510**, 518 (2014).
- [27] G. Lamporesi, A. Bertoldi, L. Cacciapuoti, M. Prevedelli, and G. M. Tino, Determination of the newtonian gravitational constant using atom interferometry, *Phys. Rev. Lett.* **100**, 050801 (2008).
- [28] R. H. Parker, C. Yu, W. Zhong, B. Estey, and H. Müller, Measurement of the fine-structure constant as a test of the standard model, *Science* **360**, 191 (2018), <https://www.science.org/doi/pdf/10.1126/science.aap7706>.
- [29] R. Bouchendira, P. Cladé, S. Guellati-Khélifa, F. m. c. Nez, and F. m. c. Biraben, New determination of the fine structure constant and test of the quantum electrodynamics, *Phys. Rev. Lett.* **106**, 080801 (2011).
- [30] P. Hamilton, M. Jaffe, P. Haslinger, Q. Simmons, H. Müller, and J. Khoury, Atom-interferometry constraints on dark energy, *Science* **349**, 849 (2015), <https://www.science.org/doi/pdf/10.1126/science.aaa8883>.
- [31] S.-w. Chiow and N. Yu, Multiloop atom interferometer measurements of chameleon dark energy in microgravity, *Physical Review D* **97**, 044043 (2018).
- [32] A. Arvanitaki, P. W. Graham, J. M. Hogan, S. Rajendran, and K. Van Tilburg, Search for light scalar dark matter with atomic gravitational wave detectors, *Phys. Rev. D* **97**, 075020 (2018).
- [33] Y. A. El-Neaj, C. Alpigiani, S. Amairi-Pyka, H. Araújo, A. Balaž, A. Bassi, L. Bathe-Peters, B. Battelier, A. Belić, E. Bentine, J. Bernabeu, A. Bertoldi, R. Bingham, D. Blas, V. Bolpasi, K. Bongs, S. Bose, P. Bouyer, T. Bowcock, W. Bowden, O. Buchmueller, C. Burrage, X. Calmet, B. Canuel, L.-I. Caramete, A. Carroll, G. Cella, V. Charmandaris, S. Chattopadhyay, X. Chen, M. L. Chiofalo, J. Coleman, J. Cotter, Y. Cui, A. Derevianko, A. De Roeck, G. S. Djordjevic, P. Dornan, M. Doser, I. Drougkakis, J. Dunningham,

- I. Dutan, S. Easo, G. Elertas, J. Ellis, M. El Sawy, F. Fassi, D. Felea, C.-H. Feng, R. Flack, C. Foot, I. Fuentes, N. Gaaloul, A. Gauguet, R. Geiger, V. Gibson, G. Giudice, J. Goldwin, O. Grachov, P. W. Graham, D. Grasso, M. van der Grinten, M. Gündogan, M. G. Haehnelt, T. Harte, A. Hees, R. Hobson, J. Hogan, B. Holst, M. Holynski, M. Kasevich, B. J. Kavanagh, W. von Klitzing, T. Kovachy, B. Krikler, M. Krutzik, M. Lewicki, Y.-H. Lien, M. Liu, G. G. Luciano, A. Magnon, M. A. Mahmoud, S. Malik, C. McCabe, J. Mitchell, J. Pahl, D. Pal, S. Pandey, D. Papazoglou, M. Paternostro, B. Penning, A. Peters, M. Prevedelli, V. Puthiya-Veetil, J. Quenby, E. Rasel, S. Ravenhall, J. Ringwood, A. Roura, D. Sabulsky, M. Sameed, B. Sauer, S. A. Schäffer, S. Schiller, V. Schkolnik, D. Schlippert, C. Schubert, H. R. Sfar, A. Shayeghi, I. Shipsey, C. Signorini, Y. Singh, M. Soares-Santos, F. Sorrentino, T. Sumner, K. Tassis, S. Tentindo, G. M. Tino, J. N. Tinsley, J. Unwin, T. Valenzuela, G. Vasilakis, V. Vaskonen, C. Vogt, A. Webber-Date, A. Wenzlawski, P. Windpassinger, M. Woltmann, E. Yazgan, M.-S. Zhan, X. Zou, and J. Zupan, Aedge: Atomic experiment for dark matter and gravity exploration in space, *EPJ Quantum Technology* **7**, 10.1140/epjqt/s40507-020-0080-0 (2020).
- [34] P. W. Graham, D. E. Kaplan, J. Mardon, S. Rajendran, and W. A. Terrano, Dark matter direct detection with accelerometers, *Phys. Rev. D* **93**, 075029 (2016).
- [35] S. Abend, B. Allard, I. Alonso, J. Antoniadis, H. Araújo, G. Arduini, A. S. Arnold, T. Asano, N. Augst, L. Badurina, *et al.*, Terrestrial very-long-baseline atom interferometry: Workshop summary, *AVS Quantum Science* **6**, 024701 (2024).
- [36] P. W. Graham, D. E. Kaplan, J. Mardon, S. Rajendran, W. A. Terrano, L. Trahms, and T. Wilkason, Spin precession experiments for light axionic dark matter, *Phys. Rev. D* **97**, 055006 (2018).
- [37] F. Di Pumpo, A. Friedrich, and E. Giese, Optimal baseline exploitation in vertical dark-matter detectors based on atom interferometry, *AVS Quantum Science* **6** (2024).
- [38] M. Abe, P. Adamson, M. Borcean, D. Bortoletto, K. Bridges, S. P. Carman, S. Chattopadhyay, J. Coleman, N. M. Curfman, K. DeRose, *et al.*, Matter-wave atomic gradiometer interferometric sensor (magis-100), *Quantum Sci. Technol.* **6**, 044003 (2021).
- [39] L. Badurina, E. Bentine, D. Blas, K. Bongs, D. Bortoletto, T. Bowcock, K. Bridges, W. Bowden, O. Buchmueller, C. Burrage, J. Coleman, G. Elertas, J. Ellis, C. Foot, V. Gibson, M. Haehnelt, T. Harte, S. Hedges, R. Hobson, M. Holynski, T. Jones, M. Langlois, S. Lelouch, M. Lewicki, R. Maiolino, P. Majewski, S. Malik, J. March-Russell, C. McCabe, D. Newbold, B. Sauer, U. Schneider, I. Shipsey, Y. Singh, M. Uchida, T. Valenzuela, M. van der Grinten, V. Vaskonen, J. Vosseveld, D. Weatherill, and I. Wilmut, Aion: an atom interferometer observatory and network, *Journal of Cosmology and Astroparticle Physics* **2020** (05), 011.
- [40] M.-S. Zhan, J. Wang, W.-T. Ni, D.-F. Gao, G. Wang, L.-X. He, R.-B. Li, L. Zhou, X. Chen, J.-Q. Zhong, B. Tang, Z.-W. Yao, L. Zhu, Z.-Y. Xiong, S.-B. Lu, G.-H. Yu, Q.-F. Cheng, M. Liu, Y.-R. Liang, P. Xu, X.-D. He, M. Ke, Z. Tan, and J. Luo, Zaiga: Zhaoshan long-baseline atom interferometer gravitation antenna, *International Journal of Modern Physics D* **29**, 1940005 (2020), <https://doi.org/10.1142/S0218271819400054>.
- [41] P. W. Graham, J. M. Hogan, M. A. Kasevich, and S. Rajendran, Resonant mode for gravitational wave detectors based on atom interferometry, *Phys. Rev. D* **94**, 104022 (2016).
- [42] A. Torres-Orjuela, Detecting intermediate-mass black hole binaries with atom interferometer observatories: Using the resonant mode for the merger phase, *AVS Quantum Science* **5** (2023).
- [43] Y. A. El-Neaj, C. Alpigiani, S. Amairi-Pyka, H. Araújo, A. Balaž, A. Bassi, L. Bathe-Peters, B. Battelier, A. Belić, E. Bentine, J. Bernabeu, A. Bertoldi, R. Bingham, *et al.*, AEDGE: Atomic Experiment for Dark Matter and Gravity Exploration in Space, *EPJ Quantum Technol.* **7**, 6 (2020).
- [44] S. Baum, Z. Bogorad, and P. W. Graham, Gravitational wave measurement in the mid-band with atom interferometers, *Journal of Cosmology and Astroparticle Physics* **2024** (05), 027.
- [45] C. Schubert, D. Schlippert, S. Abend, E. Giese, A. Roura, W. Schleich, W. Ertmer, and E. Rasel, Scalable, symmetric atom interferometer for infrasound gravitational wave detection, *arXiv preprint arXiv:1909.01951* (2019).
- [46] S. Dimopoulos, P. W. Graham, J. M. Hogan, M. A. Kasevich, and S. Rajendran, Atomic gravitational wave interferometric sensor, *Phys. Rev. D* **78**, 122002 (2008).
- [47] N. Yu and M. Tinto, Gravitational wave detection with single-laser atom interferometers, *General Relativity and Gravitation* **43**, 1943 (2011).
- [48] W. Chaibi, R. Geiger, B. Canuel, A. Bertoldi, A. Landragin, and P. Bouyer, Low frequency gravitational wave detection with ground-based atom interferometer arrays, *Phys. Rev. D* **93**, 021101 (2016).
- [49] J. M. Hogan, D. M. S. Johnson, S. Dickerson, T. Kovachy, A. Sugarbaker, S.-w. Chiow, P. W. Graham, M. A. Kasevich, B. Saif, S. Rajendran, P. Bouyer, B. D. Seery, L. Feinberg, and R. Keski-Kuha, An atomic gravitational wave interferometric sensor in low earth orbit (agis-leo), *General Relativity and Gravitation* **43**, 1953 (2011).
- [50] P. W. Graham, J. M. Hogan, M. A. Kasevich, and S. Rajendran, New method for gravitational wave detection with atomic sensors, *Phys. Rev. Lett.* **110**, 171102 (2013).
- [51] B. Canuel, S. Abend, P. Amaro-Seoane, F. Badaracco, Q. Beaufils, A. Bertoldi, K. Bongs, P. Bouyer, C. Braxmaier, W. Chaibi, N. Christensen, F. Fitzek, G. Flouris, N. Gaaloul, S. Gaffet, C. L. G. Alzar, R. Geiger, S. Guellati-Khelifa, K. Hammerer, J. Harms, J. Hinderer, M. Holynski, J. Junca, S. Katsanevas, C. Klempt, C. Kozanitis, M. Krutzik, A. Landragin, I. L. Roche, B. Leykauf, Y.-H. Lien, S. Loriani, S. Merlet, M. Merzougui, M. Nofrarias, P. Papadakos, F. P. dos Santos, A. Peters, D. Plexousakis, M. Prevedelli, E. M. Rasel, Y. Rogister, S. Rosat, A. Roura, D. O. Sabulsky, V. Schkolnik, D. Schlippert, C. Schubert, L. Sidorenkov, J.-N. Siemß, C. F. Sopena, F. Sorrentino, C. Struckmann, G. M. Tino, G. Tsagkatakis, A. Viceré, W. von Klitzing, L. Woerner, and X. Zou, Elgar—a european laboratory for gravitation and atom-interferometric research, *Classical and Quantum Gravity* **37**, 225017 (2020).

- [52] P. W. Graham, J. M. Hogan, M. A. Kasevich, S. Rajendran, and R. W. Romani, Mid-band gravitational wave detection with precision atomic sensors (2017), arXiv:1711.02225 [astro-ph.IM].
- [53] A. Bassi, K. Lochan, S. Satin, T. P. Singh, and H. Ulbricht, Models of wave-function collapse, underlying theories, and experimental tests, *Rev. Mod. Phys.* **85**, 471 (2013).
- [54] S. Nimmrichter and K. Hornberger, Macroscopicity of mechanical quantum superposition states, *Phys. Rev. Lett.* **110**, 160403 (2013).
- [55] A. Bassi, A. Großardt, and H. Ulbricht, Gravitational decoherence, *Classical and Quantum Gravity* **34**, 193002 (2017).
- [56] N. Altamirano, P. Corona-Ugalde, R. B. Mann, and M. Zych, Gravity is not a pairwise local classical channel, *Classical and Quantum Gravity* **35**, 145005 (2018).
- [57] T. Kovachy, P. Asenbaum, C. Overstreet, C. A. Donnelly, S. M. Dickerson, A. Sugarbaker, J. M. Hogan, and M. A. Kasevich, Quantum superposition at the half-metre scale, *Nature* **528**, 530 (2015).
- [58] P. Asenbaum, C. Overstreet, T. Kovachy, D. D. Brown, J. M. Hogan, and M. A. Kasevich, Phase shift in an atom interferometer due to spacetime curvature across its wave function, *Phys. Rev. Lett.* **118**, 183602 (2017).
- [59] V. Xu, M. Jaffe, C. D. Panda, S. L. Kristensen, L. W. Clark, and H. Müller, Probing gravity by holding atoms for 20 seconds, *Science* **366**, 745 (2019), <https://www.science.org/doi/pdf/10.1126/science.aay6428>.
- [60] M. Arndt and K. Hornberger, Testing the limits of quantum mechanical superpositions, *Nature Physics* **10**, 271 (2014).
- [61] M. Zych, F. Costa, I. Pikovski, and Č. Brukner, Quantum interferometric visibility as a witness of general relativistic proper time, *Nature Communications* **2**, 505 (2011).
- [62] A. Roura, Gravitational redshift in quantum-clock interferometry, *Phys. Rev. X* **10**, 021014 (2020).
- [63] D. Carney, H. Müller, and J. M. Taylor, Using an atom interferometer to infer gravitational entanglement generation, *PRX Quantum* **2**, 030330 (2021).
- [64] C. Overstreet, P. Asenbaum, J. Curti, M. Kim, and M. A. Kasevich, Observation of a gravitational aharonov-bohm effect, *Science* **375**, 226 (2022), <https://www.science.org/doi/pdf/10.1126/science.abl7152>.
- [65] P. Storey and C. Cohen-Tannoudji, The Feynman path integral approach to atomic interferometry: A tutorial, *J. Phys. II* **4**, 1999 (1994).
- [66] J. M. Hogan, D. M. S. Johnson, and M. A. Kasevich, Light-pulse atom interferometry (2008), arXiv:0806.3261 [physics.atom-ph].
- [67] G. Tino and M. Kasevich, *Atom Interferometry: Proceedings of the International School of Physics "Enrico Fermi", Course 188, Varenna on Lake Como, Villa Monastero, 15-20 July 2013*, International School of Physics Enrico Fermi Series (IOS Press, 2014).
- [68] C. Antoine and C. J. Bordé, Quantum theory of atomic clocks and gravito-inertial sensors: an update, *Journal of Optics B: Quantum and Semiclassical Optics* **5**, S199 (2003).
- [69] C. Antoine and C. Bordé, Exact phase shifts for atom interferometry, *Physics Letters A* **306**, 277 (2003).
- [70] B. Dubetsky and M. Kasevich, Atom interferometer as a selective sensor of rotation or gravity, *Physical Review A—Atomic, Molecular, and Optical Physics* **74**, 023615 (2006).
- [71] Here we consider the recoil velocity kicks v_r the matter-wave receives from absorbing/emitting a photon to not explicitly include its dependence on \hbar through the photon momentum, see Tab. I.
- [72] F. Fitzek, J.-N. Siemß, S. Seckmeyer, H. Ahlers, E. M. Rasel, K. Hammerer, and N. Gaaloul, Universal atom interferometer simulation of elastic scattering processes, *Scientific Reports* **10** (2020).
- [73] B. Dubetsky, S. B. Libby, and P. Berman, Atom interferometry in the presence of an external test mass, *Atoms* **4**, 14 (2016).
- [74] A. Bertoldi, F. Minardi, and M. Prevedelli, Phase shift in atom interferometers: Corrections for nonquadratic potentials and finite-duration laser pulses, *Physical Review A* **99**, 033619 (2019).
- [75] C. Ufrecht and E. Giese, Perturbative operator approach to high-precision light-pulse atom interferometry, *Physical Review A* **101**, 053615 (2020).
- [76] W. LaRow, M. Edwards, and C. A. Sackett, Beyond the semiclassical approximation in atom interferometry, *Phys. Rev. A* **111**, 033315 (2025), publisher: American Physical Society.
- [77] C. Burrage, C. Käding, P. Millington, and J. Minář, Open quantum dynamics induced by light scalar fields, *Phys. Rev. D* **100**, 076003 (2019), eprint: 1812.08760.
- [78] C. Käding and M. Pitschmann, New method for directly computing reduced density matrices, *Phys. Rev. D* **107**, 016005 (2023), eprint: 2204.08829.
- [79] C. Käding, M. Pitschmann, and C. Voith, Dilaton-induced open quantum dynamics, *Eur. Phys. J. C* **83**, 767 (2023), eprint: 2306.10896.
- [80] R. E. Sapiro, R. Zhang, and G. Raithel, Atom interferometry using kapitza-dirac scattering in a magnetic trap, *Phys. Rev. A* **79**, 043630 (2009).
- [81] W. Hänsel, J. Reichel, P. Hommelhoff, and T. W. Hänsch, Trapped-atom interferometer in a magnetic microtrap, *Phys. Rev. A* **64**, 063607 (2001).
- [82] T. Schumm, P. Krüger, S. Hofferberth, I. Lesanovsky, S. Wildermuth, S. Groth, I. Bar-Joseph, L. M. Andersson, and J. Schmiedmayer, A double well interferometer on an atom chip, *Quantum Information Processing* **5**, 537 (2006).
- [83] M. M. Beydler, E. R. Moan, Z. Luo, Z. Chu, and C. A. Sackett, Guided-wave Sagnac atom interferometer with large area and multiple orbits, *AVS Quantum Science* **6**, 014401 (2024), https://pubs.aip.org/avs/aqs/article-pdf/doi/10.1116/5.0173769/18292053/014401_1_5.0173769.pdf.
- [84] M. Horikoshi and K. Nakagawa, Dephasing due to atom-atom interaction in a waveguide interferometer using a bose-einstein condensate, *Phys. Rev. A* **74**, 031602 (2006).
- [85] G. Raithel, A. Duspayev, B. Dash, S. C. Carrasco, M. H. Goerz, V. Vuletić, and V. S. Malinovsky, Principles of tractor atom interferometry, *Quantum Science and Technology* **8**, 014001 (2022).
- [86] B. Dash, M. H. Goerz, A. Duspayev, S. C. Carrasco, V. S. Malinovsky, and G. Raithel, Rotation sensing using tractor atom interferometry, *AVS Quantum Science* **6**, 014407 (2024), https://pubs.aip.org/avs/aqs/article-pdf/doi/10.1116/5.0175802/19712564/014407_1_5.0175802.pdf.

- [87] G. D. McDonald, C. C. N. Kuhn, S. Bennetts, J. E. Debs, K. S. Hardman, M. Johnsson, J. D. Close, and N. P. Robins, $80\hbar k$ momentum separation with bloch oscillations in an optically guided atom interferometer, *Phys. Rev. A* **88**, 053620 (2013).
- [88] G. D. McDonald, H. Keal, P. A. Altin, J. E. Debs, S. Bennetts, C. C. N. Kuhn, K. S. Hardman, M. T. Johnsson, J. D. Close, and N. P. Robins, Optically guided linear mach-zehnder atom interferometer, *Phys. Rev. A* **87**, 013632 (2013).
- [89] K. A. Krzyzanowska, J. Ferreras, C. Ryu, E. C. Samson, and M. G. Boshier, Matter-wave analog of a fiber-optic gyroscope, *Phys. Rev. A* **108**, 043305 (2023).
- [90] H. Kim, K. Krzyzanowska, K. C. Henderson, C. Ryu, E. Timmermans, and M. Boshier, One second interrogation time in a 200 round-trip waveguide atom interferometer (2022), arXiv:2201.11888 [physics.atom-ph].
- [91] R. Charrière, M. Cadoret, N. Zahzam, Y. Bidet, and A. Bresson, Local gravity measurement with the combination of atom interferometry and bloch oscillations, *Phys. Rev. A* **85**, 013639 (2012).
- [92] C. D. Panda, M. J. Tao, M. Ceja, J. Houry, G. M. Tino, and H. Müller, Measuring gravitational attraction with a lattice atom interferometer, *Nature* 10.1038/s41586-024-07561-3 (2024).
- [93] C. D. Panda, M. Tao, J. Egelhoff, M. Ceja, V. Xu, and H. Müller, Coherence limits in lattice atom interferometry at the one-minute scale, *Nature Physics* 10.1038/s41567-024-02518-9 (2024).
- [94] T. Kovachy, J. M. Hogan, D. M. S. Johnson, and M. A. Kasevich, Optical lattices as waveguides and beam splitters for atom interferometry: An analytical treatment and proposal of applications, *Phys. Rev. A* **82**, 013638 (2010).
- [95] G. Premawardhana, J. Kunjummen, S. Subhankar, and J. M. Taylor, Feasibility of a trapped atom interferometer with accelerating optical traps, *Phys. Rev. A* **109**, 053316 (2024), publisher: American Physical Society.
- [96] J. Nemirovsky, R. Weill, I. Meltzer, and Y. Sagi, Atomic interferometer based on optical tweezers, *Phys. Rev. Res.* **5**, 043300 (2023), publisher: American Physical Society.
- [97] C. D. Panda, M. Tao, M. Ceja, A. Reynoso, and H. Müller, Atomic gravimeter robust to environmental effects, *Applied Physics Letters* **123** (2023).
- [98] M. Feit, J. Fleck, and A. Steiger, Solution of the schrödinger equation by a spectral method, *Journal of Computational Physics* **47**, 412 (1982).
- [99] M. Srednicki, *Quantum field theory* (Cambridge University Press, 2007).
- [100] A. Zee, *Quantum Field Theory in a Nutshell: Second Edition*, In a Nutshell (Princeton University Press, 2010).
- [101] M. Peskin, *An Introduction To Quantum Field Theory* (CRC Press, 2018).
- [102] R. Feynman and A. Hibbs, *Quantum Mechanics and Path Integrals*, International Earth and Planetary Sciences Series (McGraw-Hill, 1965).
- [103] This follows from the fact that $\psi^{(0)}$ is a convolution of ψ_0 and $K^{(0)}$, which are both Gaussian. Convoluting two Gaussians is equivalent to taking the inverse Fourier transform of the product of the Fourier transform of the two Gaussians. Since the Fourier transform of a Gaussian is Gaussian, and the product of two Gaussians is Gaussian, $\psi^{(0)}$ must be Gaussian.
- [104] In other words, the laser produces the superposition of interferometer arms. Without the laser, there is no superposition, and the two ‘arms’ of the interferometer will correspond to exactly the same trajectory. In this case, the phase shift between the two ‘arms’ is zero. The value of a bubble diagram is completely independent of the parameters of the laser pulse, and so has the same value as when the laser performs no atom-optic operations. In this case, the phase shift is zero, so it must be that the bubble diagrams sum to zero for all possible interferometer sequences.
- [105] B. Dubetsky, Comment on “Perturbative operator approach to high-precision light-pulse atom interferometry”, *Phys. Rev. A* **102**, 027301 (2020), publisher: American Physical Society.
- [106] C. Ufrecht and E. Giese, Reply to “Comment on ‘Perturbative operator approach to high-precision light-pulse atom interferometry’ ”, *Phys. Rev. A* **102**, 027302 (2020), publisher: American Physical Society.
- [107] J. H. T. Burke and C. A. Sackett, Scalable bose-einstein condensate sagnac interferometer in a linear trap, *Phys. Rev. A* **80**, 061603 (2009).
- [108] E. R. Moan, S. J. Berl, Z. Luo, and C. Sackett, Controlling the anharmonicity of a time-orbiting potential trap, in *OPTO* (2020).
- [109] As described in [83], an upgraded version of this apparatus has been implemented with reduced anharmonicities.
- [110] E. Moan, Z. Luo, and C. A. Sackett, A large-area Sagnac interferometer using atoms in a time-orbiting potential, in *Optical, Opto-Atomic, and Entanglement-Enhanced Precision Metrology*, Vol. 10934, edited by S. M. Shahriar and J. Scheuer, International Society for Optics and Photonics (SPIE, 2019) p. 109341X.
- [111] S. Thomas, C. Sapp, C. Henry, A. Smith, C. A. Sackett, C. W. Clark, and M. Edwards, Modeling Atom Interferometry Experiments with Bose–Einstein Condensates in Power-Law Potentials, *Atoms* **10**, 10.3390/atoms10010034 (2022).
- [112] I. Hirschman and D. Widder, *The Convolution Transform*, Dover Books on Mathematics (Dover Publications, 2012).
- [113] Y. Wang, J. Glick, T. Deshpande, K. DeRose, S. Saraf, N. Sachdeva, K. Jiang, Z. Chen, and T. Kovachy, Robust Quantum Control via Multipath Interference for Thousandfold Phase Amplification in a Resonant Atom Interferometer, *Phys. Rev. Lett.* **133**, 243403 (2024), publisher: American Physical Society.

Appendix A: Calculating Value of Diagram External and Internal Edges

To compute the value of diagram edges, it will be important to leverage two Gaussian integral identities, denoted as Eq. A1 and Eq. A2. Both of these integral identities are ultimately just extensions of the identity $\int_{-\infty}^{\infty} dx e^{-ax^2+bx} = \sqrt{\pi/a} e^{b^2/(4a)}$ for $\text{Re}[a] > 0$. The first integral identity is

$$I_1[x] = A \exp \left[x^2 G^{(0,2)} + x G^{(0,1)} + G^{(0,0)} + \int_{t_i}^{t_f} dt (x G^{(1,1)}[t] + G^{(1,0)}[t]) J[t] + \frac{1}{2} \int_{t_i}^{t_f} dt_1 \int_{t_i}^{t_f} dt_2 J[t_1] G^{(2,0)}[t_1, t_2] J[t_2] \right]$$

$$\int_{-\infty}^{\infty} dx I_1[x] = \bar{A} \exp \left[\bar{G}^{(0)} + \int_{t_i}^{t_f} dt \bar{G}^{(1)}[t] J[t] + \frac{1}{2} \int_{t_i}^{t_f} dt_1 \int_{t_i}^{t_f} dt_2 J[t_1] \bar{G}^{(2)}[t_1, t_2] J[t_2] \right] \quad (\text{A1})$$

where

$$\bar{A} = A \sqrt{\frac{\pi}{-G^{(0,2)}}}$$

$$\bar{G}^{(0)} = G^{(0,0)} - \frac{(G^{(0,1)})^2}{4G^{(0,2)}}$$

$$\bar{G}^{(1)}[t] = G^{(1,0)}[t] - \frac{G^{(0,1)}G^{(1,1)}[t]}{2G^{(0,2)}}$$

$$\bar{G}^{(2)}[t_1, t_2] = G^{(2,0)}[t_1, t_2] - \frac{G^{(1,1)}[t_1]G^{(1,1)}[t_2]}{2G^{(0,2)}}$$

and $G^{(j,k)}[t_1, t_2]$ denotes a function associated with a term in the exponent of the integrand which is j^{th} order in the integration variable x and k^{th} order in the function $J[t]$. The second integral identity concerns integrating over an expression which consists of two different source terms J_1 and J_2 :

$$I_2[x] = A \exp \left[x^2 G^{(0,2)} + x G^{(0,1)} + G^{(0,0)} + \int_{t_i}^{t_f} dt \left((x G_1^{(1,1)}[t] + G_1^{(1,0)}[t]) J_1[t] + (x G_2^{(1,1)}[t] + G_2^{(1,0)}[t]) J_2[t] \right) \right.$$

$$\left. + \frac{1}{2} \int_{t_i}^{t_f} dt_1 \int_{t_i}^{t_f} dt_2 (J_1[t_1] G_{11}^{(2,0)}[t_1, t_2] J_1[t_2] + J_2[t_1] G_{22}^{(2,0)}[t_1, t_2] J_2[t_2]) \right]$$

$$\int_{-\infty}^{\infty} dx I_2[x] = \bar{A} \exp \left[\bar{G}^{(0)} + \int_{t_i}^{t_f} dt (\bar{G}_1^{(1)}[t] J_1[t] + \bar{G}_2^{(1)}[t] J_2[t]) \right.$$

$$\left. + \frac{1}{2} \int_{t_i}^{t_f} dt_1 \int_{t_i}^{t_f} dt_2 (J_1[t_1] \bar{G}_{11}^{(2)}[t_1, t_2] J_1[t_2] + J_1[t_1] \bar{G}_{12}^{(2)}[t_1, t_2] J_2[t_2] + J_2[t_1] \bar{G}_{21}^{(2)}[t_1, t_2] J_1[t_2] + J_2[t_1] \bar{G}_{22}^{(2)}[t_1, t_2] J_2[t_2]) \right] \quad (\text{A2})$$

where

$$\bar{A} = A \sqrt{\frac{\pi}{-G^{(0,2)}}}$$

$$\bar{G}^{(0)} = G^{(0,0)} - \frac{(G^{(0,1)})^2}{4G^{(0,2)}}$$

$$\bar{G}_j^{(1)}[t] = G_j^{(1,0)}[t] - \frac{G^{(0,1)}G_j^{(1,1)}[t]}{2G^{(0,2)}} \quad , \quad j = 1, 2$$

$$\bar{G}_{jk}^{(2)}[t_1, t_2] = \delta_{jk} G_{jj}^{(2,0)}[t_1, t_2] - \frac{G_j^{(1,1)}[t_1]G_k^{(1,1)}[t_2]}{2G^{(0,2)}} \quad , \quad j, k = 1, 2$$

We will use both of these expressions to compute the value of the internal and external edges associated with a diagram. Consider the Lagrangian

$$L = \frac{1}{2} \dot{x}^2 - \frac{1}{2} m \omega^2 x^2 + J[t]x$$

for which a kernel solution can be written as [102]

$$\begin{aligned}
K^{(0)}[x_f, t_f; x_i, t_i; J[t]] &= \left(\frac{m\omega}{2\pi i \hbar \sin[\omega(t_f - t_i)]} \right)^{1/2} \\
&\times \exp \left[\frac{i}{\hbar} \frac{m\omega}{2 \sin[\omega(t_f - t_i)]} \left((x_f^2 + x_i^2) \cos[\omega(t_f - t_i)] - 2x_f x_i \right. \right. \\
&\quad \left. \left. + \frac{2}{m\omega} \int_{t_i}^{t_f} dt J[t] (x_f \sin[\omega(t - t_i)] + x_i \sin[\omega(t_f - t)]) \right. \right. \\
&\quad \left. \left. - \frac{1}{m^2 \omega^2} \int_{t_i}^{t_f} dt_1 \int_{t_i}^{t_f} dt_2 J[t_1] J[t_2] \begin{cases} \sin[\omega(t_f - t_2)] \sin[\omega(t_1 - t_i)] & , t_1 < t_2 \\ \sin[\omega(t_f - t_1)] \sin[\omega(t_2 - t_i)] & , t_1 > t_2 \end{cases} \right) \right]
\end{aligned}$$

Defining an initial wavefunction of the form

$$\psi_0[x_i, t_i] = \left(\frac{2}{\pi w_0^2} \right)^{1/4} e^{-\frac{1}{w_0^2} x_i^2}$$

Then the wavefunction at a later time t_f can be expressed as

$$\psi[x_f, t_f; J[t]] = \int_{-\infty}^{\infty} dx_i K[x_f, t_f; x_i, t_i; J[t]] \psi_0[x_i, t_i]$$

which can be solved by leveraging Eq. A1 with

$$\begin{aligned}
A &= \left(\frac{m\omega}{2\pi i \hbar \sin[\omega(t_f - t_i)]} \right)^{1/2} \left(\frac{2}{\pi w_0^2} \right)^{1/4} \\
G^{(0,2)} &= \frac{im\omega \cos[\omega(t_f - t_i)]}{2\hbar \sin[\omega(t_f - t_i)]} - \frac{1}{w_0^2} \\
G^{(0,1)} &= \frac{-im\omega x_f}{\hbar \sin[\omega(t_f - t_i)]} \\
G^{(0,0)} &= \frac{im\omega \cos[\omega(t_f - t_i)] x_f^2}{2\hbar \sin[\omega(t_f - t_i)]} \\
G^{(1,1)}[t] &= \frac{i \sin[\omega(t_f - t)]}{\hbar \sin[\omega(t_f - t_i)]} \\
G^{(1,0)}[t] &= \frac{i \sin[\omega(t - t_i)] x_f}{\hbar \sin[\omega(t_f - t_i)]} \\
G^{(2,0)}[t_1, t_2] &= \frac{-i}{m\omega \hbar \sin[\omega(t_f - t_i)]} \begin{cases} \sin[\omega(t_f - t_2)] \sin[\omega(t_1 - t_i)] & , t_1 < t_2 \\ \sin[\omega(t_f - t_1)] \sin[\omega(t_2 - t_i)] & , t_1 > t_2 \end{cases}
\end{aligned}$$

which results in

$$\psi[x_f, t_f; J[t]] = A_\psi \exp \left[x_f^2 G_\psi^{(0)} + x_f \int_{t_i}^{t_f} dt G_\psi^{(1)}[t] J[t] + \frac{1}{2} \int_{t_i}^{t_f} dt_1 \int_{t_i}^{t_f} dt_2 J[t_1] G_\psi^{(2)}[t_1, t_2] J[t_2] \right]$$

where

$$\begin{aligned}
A_\psi &= \left(\frac{2}{\pi w_0^2}\right)^{1/4} \left(\frac{\omega}{\omega \cos[\omega(t_f - t_i)] + i\beta \sin[\omega(t_f - t_i)]}\right)^{1/2} \\
G_\psi^{(0)} &= -\frac{m\omega}{2\hbar} \frac{i\omega \sin[\omega(t_f - t_i)] + \beta \cos[\omega(t_f - t_i)]}{i\beta \sin[\omega(t_f - t_i)] + \omega \cos[\omega(t_f - t_i)]} \\
G_\psi^{(1)}[t] &= \frac{i}{\hbar} \left(\frac{\sin[\omega(t - t_i)]}{\sin[\omega(t_f - t_i)]} + \frac{\omega}{\omega \cos[\omega(t_f - t_i)] + i\beta \sin[\omega(t_f - t_i)]} \frac{\sin[\omega(t_f - t)]}{\sin[\omega(t_f - t_i)]} \right) \\
G_\psi^{(2)}[t_1, t_2] &= -\frac{1}{m\hbar} \left(\frac{i}{\omega \sin[\omega(t_f - t_i)]} \begin{cases} \sin[\omega(t_f - t_2)] \sin[\omega(t_1 - t_i)] & , t_1 < t_2 \\ \sin[\omega(t_f - t_1)] \sin[\omega(t_2 - t_i)] & , t_1 > t_2 \end{cases} \right. \\
&\quad \left. + \frac{1}{\beta \sin[\omega(t_f - t_i)] - i\omega \cos[\omega(t_f - t_i)]} \frac{\sin[\omega(t_f - t_1)] \sin[\omega(t_f - t_2)]}{\sin[\omega(t_f - t_i)]} \right)
\end{aligned}$$

and $\beta = \frac{2\hbar}{mw_0^2}$. This is the integration done as part of Eq. 5 in the main text. Next we compute the expression

$$C e^{i\Delta\phi} = \int_{-\infty}^{\infty} dx_f \psi^{(0)}[x_f, t_f; J_1[t]] (\psi^{(0)}[x_f, t_f; J_2[t]])^*$$

using Eq. A2 with

$$\begin{aligned}
A &= |A_\psi|^2 \\
G^{(0,2)} &= G_\psi^{(0)} + (G_\psi^{(0)})^* \\
G^{(0,1)} &= G^{(0,0)} = 0 \\
G_1^{(1,0)}[t] &= G_2^{(1,0)}[t] = 0 \\
G_1^{(1,1)}[t] &= G_\psi^{(1)}[t] \\
G_2^{(1,1)}[t] &= (G_\psi^{(1)}[t])^* \\
G_{11}^{(2,0)}[t_1, t_2] &= G_\psi^{(2)}[t_1, t_2] \\
G_{22}^{(2,0)}[t_1, t_2] &= (G_\psi^{(2)}[t_1, t_2])^*
\end{aligned}$$

which results in

$$\begin{aligned}
C e^{i\Delta\phi} &= \exp \left[\frac{1}{2} \int_{t_i}^{t_f} dt_1 \int_{t_i}^{t_f} dt_2 \left(\begin{aligned} &J_1[t_1] G_{11}[t_1, t_2] J_1[t_2] \\ &+ J_1[t_1] G_{12}[t_1, t_2] J_2[t_2] \\ &+ J_2[t_1] G_{21}[t_1, t_2] J_1[t_2] \\ &+ J_2[t_1] G_{22}[t_1, t_2] J_2[t_2] \end{aligned} \right) \right]
\end{aligned} \tag{A3}$$

with

$$\begin{aligned}
G_{11}[t_1, t_2] &= \frac{1}{2m\hbar} \left(-\frac{\beta \sin[\omega(t_1 - t_i)] \sin[\omega(t_2 - t_i)]}{\omega^2} - \frac{\cos[\omega(t_1 - t_i)] \cos[\omega(t_2 - t_i)]}{\beta} + i \frac{\sin[\omega|t_1 - t_2|]}{\omega} \right) \\
G_{12}[t_1, t_2] &= \frac{1}{2m\hbar} \left(\frac{\beta \sin[\omega(t_1 - t_i)] \sin[\omega(t_2 - t_i)]}{\omega^2} + \frac{\cos[\omega(t_1 - t_i)] \cos[\omega(t_2 - t_i)]}{\beta} + i \frac{\sin[\omega(t_1 - t_2)]}{\omega} \right) \\
G_{21}[t_1, t_2] &= \frac{1}{2m\hbar} \left(\frac{\beta \sin[\omega(t_1 - t_i)] \sin[\omega(t_2 - t_i)]}{\omega^2} + \frac{\cos[\omega(t_1 - t_i)] \cos[\omega(t_2 - t_i)]}{\beta} - i \frac{\sin[\omega(t_1 - t_2)]}{\omega} \right) \\
G_{22}[t_1, t_2] &= \frac{1}{2m\hbar} \left(-\frac{\beta \sin[\omega(t_1 - t_i)] \sin[\omega(t_2 - t_i)]}{\omega^2} - \frac{\cos[\omega(t_1 - t_i)] \cos[\omega(t_2 - t_i)]}{\beta} - i \frac{\sin[\omega|t_1 - t_2|]}{\omega} \right)
\end{aligned} \tag{A4}$$

In Sec. II B, we simplify the notation of Eq. A3 by expressing it as

$$C e^{i\Delta\phi} = \exp \left[\frac{1}{2} \int_{t_i}^{t_f} dt_1 \int_{t_i}^{t_f} dt_2 J_a[t_1] G_{ab}[t_1, t_2] J_b[t_2] \right]$$

where Latin indices can have value 1 or 2 and summation over repeated indices is assumed. This is the integration that is done as part of Eq. 3 in the main text. Note that performing the integration this way results in $G_{ab}[t_j, t_k] = G_{ba}[t_k, t_j]$, which is a necessary symmetry of the propagator, akin to the property $G[x_1, x_2] = G[x_2, x_1]$ in QFT. To arrive at the expression for the propagators $G_{ab}[t_1, t_2]$ in Sec. IIIB, we take $t_i = 0$, and to arrive at the the propagators of Sec. IIIA we take the limit that $\omega \rightarrow 0$.

Now we compute the value of the external edge $G_a[t] = \int_{t_i}^{t_f} dt' J_{a'}[t'] G_{a'a}[t', t]$, which depends on the form of the effective force $J_a[t]$. In this paper, we consider two different pulse sequences, corresponding to two different choices of J_a ; A Mach-Zehnder pulse sequence, as in Eq. 10

$$\frac{J_a[t]}{m} = -g + \begin{cases} v_r \delta[t-0] - v_r \delta[t-T], & a = 1 \\ v_r \delta[t-T] - v_r \delta[t-2T], & a = 2 \end{cases}$$

and a sequence where the two arms of the interferometer are kicked symmetrically as in Eq. 12.

$$\frac{J_a[t]}{m} = -g + \begin{cases} 2v_r \delta[t-0] - 4v_r \delta[t-T] + 2v_r \delta[t-2T] & a = 1 \\ -2v_r \delta[t-0] + 4v_r \delta[t-T] - 2v_r \delta[t-2T] & a = 2 \end{cases}$$

For the Mach Zehnder sequence, the value of the external edge $G_a[t]$ is given by

$$\begin{aligned} G_1[t] &= \left(-\frac{2ig}{\hbar\omega^2} \right) \left(\sin[\omega t/2]^2 \right) + \left(\frac{iv_r}{2\hbar\omega} \right) \left(\sin[\omega|t|] + \sin[\omega(t-T)] - \sin[\omega|t-T|] - \sin[\omega(t-2T)] \right) \\ &+ \left(\frac{iv_z}{2\hbar\omega} \right) \left(\sin[\omega t] + \sin[\omega|t|] \right) + \left(\frac{2v_r}{\hbar\beta} \right) \left(\cos[\omega t] \cos[\omega T] \sin[\omega T/2]^2 \right) + \left(\frac{2v_r\beta}{\hbar\omega^2} \right) \left(\sin[\omega t] \sin[\omega T] \sin[\omega T/2]^2 \right) \\ G_2[t] &= \left(\frac{2ig}{\hbar\omega^2} \right) \left(\sin[\omega t/2]^2 \right) + \left(-\frac{iv_r}{2\hbar\omega} \right) \left(\sin[\omega t] - \sin[\omega(t-T)] + \sin[\omega|t-T|] - \sin[\omega|t-2T|] \right) \\ &+ \left(-\frac{iv_z}{2\hbar\omega} \right) \left(\sin[\omega t] + \sin[\omega|t|] \right) + \left(-\frac{2v_r}{\hbar\beta} \right) \left(\cos[\omega t] \cos[\omega T] \sin[\omega T/2]^2 \right) + \left(-\frac{2v_r\beta}{\hbar\omega^2} \right) \left(\sin[\omega t] \sin[\omega T] \sin[\omega T/2]^2 \right) \end{aligned} \quad (\text{A5})$$

where we have evaluated the integral in Mathematica and expressed the result using absolute value functions. For the symmetrically kicked sequence, external edges have value

$$\begin{aligned} G_1[t] &= \left(-\frac{2ig}{\hbar\omega^2} \right) \left(\sin[\omega t/2]^2 \right) \\ &+ \left(-\frac{iv_r}{\hbar\omega} \right) \left(\sin[\omega t] - \sin[\omega|t|] - 2\sin[\omega(t-T)] + 2\sin[\omega|t-T|] + \sin[\omega(t-2T)] - \sin[\omega|t-2T|] \right) \\ &+ \left(\frac{iv_z}{2\hbar\omega} \right) \left(\sin[\omega t] + \sin[\omega|t|] \right) + \left(\frac{8v_r}{\hbar\beta} \right) \left(\cos[\omega t] \cos[\omega T] \sin[\omega T/2]^2 \right) + \left(\frac{8v_r\beta}{\hbar\omega^2} \right) \left(\sin[\omega t] \sin[\omega T] \sin[\omega T/2]^2 \right) \\ G_2[t] &= \left(\frac{2ig}{\hbar\omega^2} \right) \left(\sin[\omega t/2]^2 \right) \\ &+ \left(-\frac{iv_r}{\hbar\omega} \right) \left(\sin[\omega t] - \sin[\omega|t|] - 2\sin[\omega(t-T)] + 2\sin[\omega|t-T|] + \sin[\omega(t-2T)] - \sin[\omega|t-2T|] \right) \\ &+ \left(-\frac{iv_z}{2\hbar\omega} \right) \left(\sin[\omega t] + \sin[\omega|t|] \right) + \left(-\frac{8v_r}{\hbar\beta} \right) \left(\cos[\omega t] \cos[\omega T] \sin[\omega T/2]^2 \right) + \left(-\frac{8v_r\beta}{\hbar\omega^2} \right) \left(\sin[\omega t] \sin[\omega T] \sin[\omega T/2]^2 \right) \end{aligned} \quad (\text{A6})$$

For both sequences, in the limit $\omega \rightarrow 0$, the edge values can be expressed in terms of the unperturbed classical trajectory, as written in Eq. 11.

$$\begin{aligned} G_1[t] &= \frac{i}{\hbar} x_{\text{cl},1}^{(0)}[t] \\ G_2[t] &= -\frac{i}{\hbar} x_{\text{cl},2}^{(0)}[t] \end{aligned}$$

where $x_{\text{cl},1}^{(0)}[t]$ is the unperturbed classical trajectory of the ‘upper’ interferometer arm, and $x_{\text{cl},2}^{(0)}[t]$ is the unperturbed classical trajectory of the ‘lower’ interferometer arm. For example, for the Mach Zehnder sequence of Eq. (A5), in the limit that $\omega \rightarrow 0$, we have

$$\begin{aligned} x_{\text{cl},1}^{(0)}[t] &= -\frac{1}{2}gt^2 + \frac{1}{2}v_r(T + |t| - |t - T|) + \frac{1}{2}v_z(t + |t|) \\ &= -\frac{1}{2}gt^2 + (v_z + v_r)\Thetat - 0 + (-v_r)\Thetat - T \\ x_{\text{cl},2}^{(0)}[t] &= -\frac{1}{2}gt^2 + \frac{1}{2}v_r(T + |t - T| - |t - 2T|) + \frac{1}{2}v_z(t + |t|) \\ &= -\frac{1}{2}gt^2 + (v_z)\Thetat - 0 + (v_r)\Thetat - T + (-v_r)\Thetat - 2T \end{aligned}$$

where $\Theta[t]$ is the Heaviside theta function.

Appendix B: Calculating Diagram Vertex Values in 1D

Here we will validate the expression for the vertex value (Eq. 8) by mirroring a method by which vertex values can be computed in QFT. We will take Taylor expansions and functional derivatives to manually compute the value of a tree level (loop-free) 1-vertex diagram, then extract the value associated with the vertex of that diagram. Consider Eq. 1, rewritten here as

$$\langle 0|0\rangle_J = e^{i \int d^4x \epsilon \mathcal{L}_1 \left[\frac{1}{i} \frac{\delta}{\delta J[x]} \right]} Z_0[J] \quad (\text{B1})$$

with

$$Z_0[J] = e^{\frac{i}{2} \int d^4x_1 \int d^4x_2 J[x_1] G[x_1, x_2] J[x_2]}$$

One way to determine the value of a vertex for the diagrams which compose the solution to $\langle 0|0\rangle_J$ is to Taylor expand Z_0 and the functional in Eq. B1, then apply functional derivatives to compose a first order tree level diagram manually.

Consider the interaction term $\mathcal{L}_1 = \frac{\epsilon n}{n!} \varphi^n$. It happens that the tree level diagram that is first order in ϵ will emerge from the 1st order Taylor series coefficient of the functional in Eq. B1, and the n^{th} order Taylor series coefficients of $Z_0[J]$. These two terms can be written as

$$\left(\int d^4x \frac{i\epsilon n}{n!} \left(\frac{1}{i} \frac{\delta}{\delta J[x]} \right)^n \right) \left(\frac{1}{n!} \left(\frac{i}{2} \int d^4x_1 \int d^4x_2 J[x_1] G[x_1, x_2] J[x_2] \right)^n \right)$$

Using the identities $\frac{\delta}{\delta J[x]} J[x_1] = \delta[x - x_1]$ and $G[x_1, x_2] = G[x_2, x_1]$, the result of applying one functional derivative to the functional can be written using the identity

$$\begin{aligned}
& \frac{\delta}{\delta J[x]} \left(\int d^4 x_1 \int d^4 x_2 J[x_1] G[x_1, x_2] J[x_2] \right)^n \\
&= \frac{\delta}{\delta J[x]} \iint \dots \int d^4 x_1 d^4 x_2 \dots d^4 x_{2n-1} d^4 x_{2n} (J[x_1] G[x_1, x_2] J[x_2]) \dots (J[x_{2n-1}] G[x_{2n-1}, x_{2n}] J[x_{2n}]) \\
&= \iint \dots \int d^4 x_1 d^4 x_2 \dots d^4 x_{2n-1} d^4 x_{2n} \left((\delta[x - x_1] G[x_1, x_2] J[x_2]) \dots (J[x_{2n-1}] G[x_{2n-1}, x_{2n}] J[x_{2n}]) \right. \\
&\quad \left. + (J[x_1] G[x_1, x_2] \delta[x - x_2]) \dots (J[x_{2n-1}] G[x_{2n-1}, x_{2n}] J[x_{2n}]) \right. \\
&\quad \quad \quad \vdots \\
&\quad \left. + (J[x_1] G[x_1, x_2] J[x_2]) \dots (\delta[x - x_{2n-1}] G[x_{2n-1}, x_{2n}] J[x_{2n}]) \right. \\
&\quad \left. + (J[x_1] G[x_1, x_2] J[x_2]) \dots (J[x_{2n-1}] G[x_{2n-1}, x_{2n}] \delta[x - x_{2n}]) \right) \\
&= \iint \dots \int d^4 x_2 \dots d^4 x_{2n-1} d^4 x_{2n} (G[x, x_2] J[x_2]) \dots (J[x_{2n-1}] G[x_{2n-1}, x_{2n}] J[x_{2n}]) \\
&\quad + \iint \dots \int d^4 x_1 \dots d^4 x_{2n-1} d^4 x_{2n} (J[x_1] G[x_1, x]) \dots (J[x_{2n-1}] G[x_{2n-1}, x_{2n}] J[x_{2n}]) \\
&\quad \quad \quad \vdots \\
&\quad + \iint \dots \int d^4 x_1 d^4 x_2 \dots d^4 x_{2n} (J[x_1] G[x_1, x_2] J[x_2]) \dots (G[x, x_{2n}] J[x_{2n}]) \\
&\quad + \iint \dots \int d^4 x_1 d^4 x_2 \dots d^4 x_{2n-1} (J[x_1] G[x_1, x_2] J[x_2]) \dots (J[x_{2n-1}] G[x_{2n-1}, x]) \\
&= 2n \iint \dots \int d^4 x_1 d^4 x_2 \dots d^4 x_{2n-1} (J[x_1] G[x_1, x_2] J[x_2]) \dots (J[x_{2n-1}] G[x_{2n-1}, x]) \\
&= \left(\int d^4 x_1 \int d^4 x_2 J[x_1] G[x_1, x_2] J[x_2] \right)^{n-1} 2n \left(\int d^4 x_3 J[x_3] G[x_3, x] \right)
\end{aligned}$$

as

$$\left(\int d^4 x \frac{\epsilon c_n}{i^{n-1} n!} \left(\frac{\delta}{\delta J[x]} \right)^{n-1} \right) \underbrace{\left(\frac{i^n}{2^n n!} \left(\int d^4 x_1 \int d^4 x_2 J[x_1] G[x_1, x_2] J[x_2] \right)^{n-1} \right)}_{\text{factor 1}} \underbrace{2n \left(\int d^4 x_3 J[x_3] G[x_3, x] \right)^1}_{\text{factor 2}}$$

where the factor of $2n$ comes from the $2n$ J functions that are acted on by $\delta/\delta J[x]$. Now consider applying another functional derivative to ‘factor 1’ (applying it to ‘factor 2’ would result in a loop in the diagram, and we are aiming to construct just the tree level diagram). This results in

$$\left(\int d^4 x \frac{\epsilon c_n}{i^{n-1} n!} \left(\frac{\delta}{\delta J[x]} \right)^{n-2} \right) \underbrace{\left(\frac{i^n}{2^n n!} \left(\int d^4 x_1 \int d^4 x_2 J[x_1] G[x_1, x_2] J[x_2] \right)^{n-2} \right)}_{\text{factor 1}} 2^2 n(n-1) \underbrace{\left(\int d^4 x_3 J[x_3] G[x_3, x] \right)^2}_{\text{factor 2}}$$

Then if we keep applying functional derivatives ‘factor 1’ until we are out of functional derivatives, we will be left with

$$\left(\int d^4 x \frac{\epsilon c_n}{i^{n-1} n!} \right) \left(\frac{i^n}{2^n n!} 2^n n! \left(\int d^4 x_3 J[x_3] G[x_3, x] \right)^n \right) = \frac{1}{n!} \frac{\epsilon c_n}{i^{n-1}} \int d^4 x (iG[x])^n$$

where $G[x] = \int d^4 x' J[x'] G[x', x]$. Since this one-vertex tree level diagram is going to have symmetry factor $1/n!$ And we define the value of all the external edges which contribute to the diagram to be $(iG[x])^n$. We have therefore determined that the value of the vertex is equal to $\frac{\epsilon c_n}{i^{n-1}} \int d^4 x$, as written in Sec. II A.

Now we apply the same analysis to the diagrams which compose phase shifts in matter wave interferometry. We consider the expression of Eq. 6, re-written here as

$$C e^{i\Delta\phi} = \exp \left[\int_{t_i}^{t_f} dt_1 \epsilon \left(\underbrace{\frac{i}{\hbar} \delta_{a1} L_1 \left[\frac{\hbar}{i} \frac{\delta}{\delta J_a[t_1]} \right]}_{\text{term 1}} + \underbrace{\frac{-i}{\hbar} \delta_{a2} L_1 \left[\frac{\hbar}{-i} \frac{\delta}{\delta J_a[t_1]} \right]}_{\text{term 2}} \right) \right] Z_0[J] \quad (\text{B2})$$

with

$$Z_0[J] = e^{\frac{1}{2} \int_{t_i}^{t_f} dt_1 \int_{t_i}^{t_f} dt_2 J_b[t_1] G_{bc}[t_1, t_2] J_c[t_2]}$$

We first consider applying the functional derivatives of 'term 1'. Consider an L_1 of the form $L_1 = \frac{c_n}{n!} z^n$, the contribution to the tree level one-vertex diagram will come from the first order expansion of the functional in Eq. B2, and the n^{th} order expansion of $Z_0[J]$:

$$\left(\epsilon \int_{t_i}^{t_f} dt \frac{i}{\hbar} \delta_{a1} \frac{c_n}{n!} \left(\frac{\hbar}{i} \frac{\delta}{\delta J_a[t]} \right)^n \right) \left(\frac{1}{n!} \left(\frac{1}{2} \int_{t_i}^{t_f} dt_1 \int_{t_i}^{t_f} dt_2 J_b[t_1] G_{bc}[t_1, t_2] J_c[t_2] \right)^n \right)$$

Now using the identities $\frac{\delta}{\delta J_a[t]} J_b[t_1] = \delta_{ab} \delta[t - t_1]$ and $G_{ab}[t_1, t_2] = G_{ba}[t_2, t_1]$, the result of applying one functional derivative from the left hand side to the functional on the right hand side can be expressed as

$$\left(\int_{t_i}^{t_f} dt \frac{\epsilon c_n}{n!} \left(\frac{\hbar}{i} \right)^{n-1} \delta_{a1} \left(\frac{\delta}{\delta J_a[t]} \right)^{n-1} \right) \times \left(\frac{1}{n! 2^n} \underbrace{\left(\int_{t_i}^{t_f} dt_1 \int_{t_i}^{t_f} dt_2 J_b[t_1] G_{bc}[t_1, t_2] J_c[t_2] \right)^{n-1}}_{\text{factor 1}} \delta_{ae} 2n \underbrace{\left(\int_{t_i}^{t_f} dt_3 J_d[t_3] G_{de}[t_3, t] \right)^1}_{\text{factor 2}} \right)$$

where the factor of $2n$ emerges in the same way it did in the QFT case. After applying all functional derivatives to 'factor 1' as before, we arrive at

$$\left(\int_{t_i}^{t_f} dt \frac{\epsilon c_n}{n!} \left(\frac{\hbar}{i} \right)^{n-1} \delta_{a1} \right) \left(\frac{1}{n! 2^n} \delta_{ae} 2^n n! \left(\int_{t_i}^{t_f} dt_3 J_d[t_3] G_{de}[t_3, t] \right)^n \right) = \frac{1}{n!} \epsilon c_n \left(\frac{\hbar}{i} \right)^{n-1} \delta_{a1} \int_{t_i}^{t_f} dt G_a[t]^n$$

where $G_a[t] = \int_{t_i}^{t_f} dt' J_{a'} G_{a'a}[t', t]$. The symmetry factor of the diagram is $1/n!$. And the value of all the external edges are $G_a[t]^n$, so the vertex value is given by $\epsilon c_n \left(\frac{\hbar}{i} \right)^{n-1} \delta_{a1} \int_{t_i}^{t_f} dt$. Doing the same analysis with 'term 2' in Eq. B2 results in a vertex value of $\epsilon c_n \left(\frac{\hbar}{-i} \right)^{n-1} \delta_{a2} \int_{t_i}^{t_f} dt$. It happens that even beyond the first order expansion in ϵ , these two separate vertex values can be combined into a single vertex whose value is a sum of the two. The rest of this section will illustrate this concept. Let us first consider these two terms ('term 1' and 'term 2') in Eq. B2 to contribute two distinct vertices. We can draw the vertex associated with 'term 1' with a filled-in circle, and the vertex associated with 'term 2' as a hollow circle:

$$\begin{array}{c} \left. \begin{array}{l} \text{filled circle} \\ \text{with } n \text{ dashed lines} \end{array} \right\} n \text{ edges} \\ t, a \end{array} = \eta_{a1}^n \int_{t_i}^{t_f} dt \quad \begin{array}{c} \left. \begin{array}{l} \text{hollow circle} \\ \text{with } n \text{ dashed lines} \end{array} \right\} n \text{ edges} \\ t, a \end{array} = \eta_{a2}^n \int_{t_i}^{t_f} dt$$

where

$$\eta_{jk}^n = \epsilon c_n \left(\frac{\hbar}{i(-1)^{k+1}} \right)^{n-1} \delta_{jk}$$

Consider a diagram with m vertices indexed by $i = 1, 2, \dots, m$, where vertex i is an n_i -point vertex. Such a diagram will emerge from taking the following functional derivatives of $Z_0[J]$ in Eq. B2.

$$\begin{aligned} & \prod_{i=1}^m \frac{1}{n_i!} \int_{t_i}^{t_f} dt_i \left(\eta_{a_i 1}^{n_i} \left(\frac{\delta}{\delta J_{a_i}[t_i]} \right)^{n_i} + \eta_{a_i 2}^{n_i} \left(\frac{\delta}{\delta J_{a_i}[t_i]} \right)^{n_i} \right) \\ &= \frac{1}{\prod_{i=1}^m n_i!} \left(\int_{t_1}^{t_f} dt_1 \int_{t_2}^{t_f} dt_2 \dots \int_{t_m}^{t_f} dt_m \right) \sum_{b_1, b_2, \dots, b_m \in \{1, 2\}} \prod_{i=1}^m \eta_{a_i b_i}^{n_i} \left(\frac{\delta}{\delta J_{a_i}[t_i]} \right)^{n_i} \end{aligned}$$

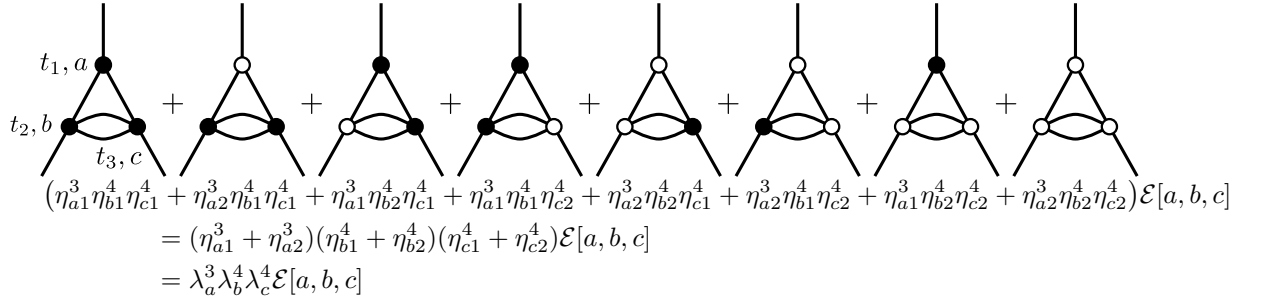
where the sum is over all the 2^m combinations of b_1, b_2, \dots, b_m , with each taking the values of 1 or 2, and vertex i is labeled ' t_i, a_i ' for $i = 1, 2, \dots, m$. The sum comes from expanding out all the terms in the product over i in the left hand side. Consider a diagram that comes out of one of the elements in this sum, corresponding to one possible set of values for b_1, b_2, \dots, b_m . We can express the value of this diagram as

$$\left(\prod_{i=1}^m \eta_{a_i b_i}^{n_i} \right) \mathcal{E}[a_1, a_2, \dots, a_m]$$

where included in the function \mathcal{E} are the edge values, the symmetry factor of the diagram, and the integrals over time associated with the vertices. The sum over the possible values of b_1, b_2, \dots, b_m can be written as

$$\sum_{b_1, b_2, \dots, b_m \in \{1, 2\}} \left(\prod_{i=1}^m \eta_{a_i b_i}^{n_i} \right) \mathcal{E}[a_1, a_2, \dots, a_m] = \left(\prod_{i=1}^m (\eta_{a_i 1}^{n_i} + \eta_{a_i 2}^{n_i}) \right) \mathcal{E}[a_1, a_2, \dots, a_m] = \left(\prod_{i=1}^m \lambda_{a_i}^{n_i} \right) \mathcal{E}[a_1, a_2, \dots, a_m]$$

where $\lambda_a^n = \eta_{a 1}^n + \eta_{a 2}^n$, so that the value of each of the m vertices can be expressed as a sum of the corresponding hollow or filled-in n_i -point vertices. As an example, consider a perturbative potential $L_1 = \frac{c_3}{3!} z^3 + \frac{c_4}{4!} z^4$, and a diagram which contributes to the phase shift at first order in c_3 and second order in c_4 under this potential. In this case, $m = 3$, and we label vertices so that $n_1 = 3, n_2 = n_3 = 4$. For notational convenience, we write $a_1 = a, a_2 = b, a_3 = c$. The 2^3 different possible values of b_1, b_2 , and b_3 will produce 8 diagrams, whose sum can be written as

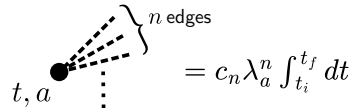


$$\begin{aligned} & (\eta_{a_1}^3 \eta_{b_1}^4 \eta_{c_1}^4 + \eta_{a_2}^3 \eta_{b_1}^4 \eta_{c_1}^4 + \eta_{a_1}^3 \eta_{b_2}^4 \eta_{c_1}^4 + \eta_{a_1}^3 \eta_{b_1}^4 \eta_{c_2}^4 + \eta_{a_2}^3 \eta_{b_2}^4 \eta_{c_1}^4 + \eta_{a_2}^3 \eta_{b_1}^4 \eta_{c_2}^4 + \eta_{a_1}^3 \eta_{b_2}^4 \eta_{c_2}^4 + \eta_{a_2}^3 \eta_{b_2}^4 \eta_{c_2}^4) \mathcal{E}[a, b, c] \\ &= (\eta_{a_1}^3 + \eta_{a_2}^3) (\eta_{b_1}^4 + \eta_{b_2}^4) (\eta_{c_1}^4 + \eta_{c_2}^4) \mathcal{E}[a, b, c] \\ &= \lambda_a^3 \lambda_b^4 \lambda_c^4 \mathcal{E}[a, b, c] \end{aligned}$$

with

$$\mathcal{E}[a, b, c] = \frac{1}{4} \int_{t_i}^{t_f} dt_1 \int_{t_i}^{t_f} dt_2 \int_{t_i}^{t_f} dt_3 (G_a[t_1] G_b[t_2] G_c[t_3] G_{bc}[t_2, t_3]^2 G_{ba}[t_2, t_1] G_{ca}[t_3, t_1])$$

where the factor of $1/4$ comes from the symmetry factor of the diagram. The two terms in Eq. B2 (referred to as 'term 1' and 'term 2'), can therefore be associated with a single vertex, rather than two distinct ones. The vertex value associated with the perturbative term $L_1 = \frac{c_n}{n!} z^n$ can be written as



$$= c_n \lambda_a^n \int_{t_i}^{t_f} dt$$

where

$$\lambda_a^n = \epsilon c_n \left(\left(\frac{\hbar}{i} \right)^{n-1} \delta_{a1} + \left(\frac{\hbar}{-i} \right)^{n-1} \delta_{a2} \right)$$

as is expressed in Eq. 8.

Appendix C: Calculating Value of Diagram External and Internal Edges in 3D

In this paper, we will make the simplifying assumption that the unperturbed Lagrangian is separable, as stated in Sec. II C

$$L_0[\dot{x}, x, \dot{y}, y, \dot{z}, z] = L_x[\dot{x}, x] + L_y[\dot{y}, y] + L_z[\dot{z}, z]$$

This way, the analysis of Sec A can be applied to each of the three cartesian dimensions individually, where the 2 point correlation functions G can be expressed as

$$G_{ab}^{\alpha\beta}[t_1, t_2] = G_{ab}^{11}[t_1, t_2]\delta_{\alpha 1}\delta_{\beta 1} + G_{ab}^{22}[t_1, t_2]\delta_{\alpha 2}\delta_{\beta 2} + G_{ab}^{33}[t_1, t_2]\delta_{\alpha 3}\delta_{\beta 3}$$

where the values of $G_{ab}^{\alpha\alpha}[t_1, t_2]$ are equal to the value of the 1D $G_{ab}[t_1, t_2]$ of Eq. (A4), but with $\beta = \beta_\alpha, \omega = \omega_\alpha$ to account for the fact that the trap stiffness and initial wavepacket sizes could be different in the different cartesian dimensions. To write this out explicitly, if we have an unperturbed Lagrangian of the form

$$L_0 = \frac{m}{2} (\dot{x}^2 + \dot{y}^2 + \dot{z}^2) - \frac{m}{2} (\omega_x^2 x^2 + \omega_y^2 y^2 + \omega_z^2 z^2)$$

then the values of $G_{ab}^{\alpha\alpha}[t_1, t_2]$ are given by

$$\begin{aligned} G_{11}^{\alpha\alpha}[t_1, t_2] &= \frac{1}{2m\hbar} \left(-\frac{\beta_\alpha \sin[\omega_\alpha(t_1 - t_i)] \sin[\omega_\alpha(t_2 - t_i)]}{\omega_\alpha^2} - \frac{\cos[\omega_\alpha(t_1 - t_i)] \cos[\omega_\alpha(t_2 - t_i)]}{\beta_\alpha} + i \frac{\sin[\omega_\alpha(t_1 - t_2)]}{\omega_\alpha} \right) \\ G_{12}^{\alpha\alpha}[t_1, t_2] &= \frac{1}{2m\hbar} \left(\frac{\beta_\alpha \sin[\omega_\alpha(t_1 - t_i)] \sin[\omega_\alpha(t_2 - t_i)]}{\omega_\alpha^2} + \frac{\cos[\omega_\alpha(t_1 - t_i)] \cos[\omega_\alpha(t_2 - t_i)]}{\beta_\alpha} + i \frac{\sin[\omega_\alpha(t_1 - t_2)]}{\omega_\alpha} \right) \\ G_{21}^{\alpha\alpha}[t_1, t_2] &= \frac{1}{2m\hbar} \left(\frac{\beta_\alpha \sin[\omega_\alpha(t_1 - t_i)] \sin[\omega_\alpha(t_2 - t_i)]}{\omega_\alpha^2} + \frac{\cos[\omega_\alpha(t_1 - t_i)] \cos[\omega_\alpha(t_2 - t_i)]}{\beta_\alpha} - i \frac{\sin[\omega_\alpha(t_1 - t_2)]}{\omega_\alpha} \right) \\ G_{22}^{\alpha\alpha}[t_1, t_2] &= \frac{1}{2m\hbar} \left(-\frac{\beta_\alpha \sin[\omega_\alpha(t_1 - t_i)] \sin[\omega_\alpha(t_2 - t_i)]}{\omega_\alpha^2} - \frac{\cos[\omega_\alpha(t_1 - t_i)] \cos[\omega_\alpha(t_2 - t_i)]}{\beta_\alpha} - i \frac{\sin[\omega_\alpha(t_1 - t_2)]}{\omega_\alpha} \right) \end{aligned}$$

where $\alpha = 1, 2, 3$ corresponding to the three cartesian dimensions, and $\omega_x = \omega_1, \omega_y = \omega_2, \omega_z = \omega_3$. It happens that this function can be written more compactly in terms of Pauli matrices in the subspace indexed by the Latin indices.

$$\begin{aligned} \mathbf{G}^{\alpha\alpha}[t_1, t_2] &= \frac{1}{2m\hbar} \left((\boldsymbol{\sigma}_1 - \mathbf{1}) \left(\frac{\beta_\alpha \sin[\omega_\alpha(t_1 - t_i)] \sin[\omega_\alpha(t_2 - t_i)]}{\omega_\alpha^2} + \frac{\cos[\omega_\alpha(t_1 - t_i)] \cos[\omega_\alpha(t_2 - t_i)]}{\beta_\alpha} \right) \right. \\ &\quad \left. + i\boldsymbol{\sigma}_3 \frac{\sin[\omega_\alpha(t_1 - t_2)]}{\omega_\alpha} - \boldsymbol{\sigma}_2 \frac{\sin[\omega_\alpha(t_1 - t_2)]}{\omega_\alpha} \right) \end{aligned}$$

where the Pauli matrices are

$$\boldsymbol{\sigma}_1 = \begin{pmatrix} 0 & 1 \\ 1 & 0 \end{pmatrix}, \quad \boldsymbol{\sigma}_2 = \begin{pmatrix} 0 & -i \\ i & 0 \end{pmatrix}, \quad \boldsymbol{\sigma}_3 = \begin{pmatrix} 1 & 0 \\ 0 & -1 \end{pmatrix}, \quad \mathbf{1} = \begin{pmatrix} 1 & 0 \\ 0 & 1 \end{pmatrix}$$

Then we have $G_{jk}^{12}[t_1, t_2] = G_{jk}^{21}[t_1, t_2] = G_{jk}^{13}[t_1, t_2] = G_{jk}^{31}[t_1, t_2] = G_{jk}^{23}[t_1, t_2] = G_{jk}^{32}[t_1, t_2] = 0$, since there are no cross terms for the position dependent coordinates in the unperturbed Lagrangian L_0 . The values of the $G_a^\alpha[t]$ can be written

$$G_a^\alpha[t] = \int_{t_i}^{t_f} dt' J_{a'}^{\alpha'}[t'] G_{a'}^{\alpha'\alpha}[t', t]$$

For an interferometer beam oriented along z , $G_a^3[t]$ has the same form as the 1D expressions of Eq. (A5) for a Mach-Zehnder interferometer sequence, and of Eq. (A6) for the symmetrically kicked interferometer sequence, where $\beta = \beta_3$ and $\omega = \omega_3$. Since the interferometer beam is oriented only along z , we have $J_a^1[t] = J_a^2[t] = 0$ so that

$G_a^1[t] = G_a^2[t] = 0$. When we include nonzero initial kinematics, (either nonzero initial transverse positions x_0 or y_0 or initial transverse velocities v_x or v_y), $G_a^1[t]$ and $G_a^2[t]$ can become nonzero. In the limit that $\omega_x \rightarrow 0$ and $\omega_y \rightarrow 0$,

$$\begin{aligned} G_a^1[t] &= (-1)^{a+1} \frac{i}{\hbar} x_{\text{cl},a}^{(0)}[t] \\ G_a^2[t] &= (-1)^{a+1} \frac{i}{\hbar} y_{\text{cl},a}^{(0)}[t] \end{aligned}$$

where if the interferometer beam is oriented along the z -axis, then

$$\begin{aligned} x_{\text{cl},a}^{(0)}[t] &= x_0 + v_x(t - t_i) \\ y_{\text{cl},a}^{(0)}[t] &= y_0 + v_y(t - t_i) \end{aligned}$$

Appendix D: Calculating Diagram Vertex Values in 3D

Here we will follow the same steps as Sec. B, using the 3D rules. The 3D version of Eq. (6) can be expressed as

$$\begin{aligned} C e^{i\Delta\phi} &= \exp \left[\int_{t_i}^{t_f} dt_1 \epsilon \left(\underbrace{\frac{i}{\hbar} \delta_{a1} L_1 \left[\frac{\hbar}{i} \delta_{\alpha 1} \frac{\delta}{\delta J_a^\alpha[t_1]}, \frac{\hbar}{i} \delta_{\alpha 2} \frac{\delta}{\delta J_a^\alpha[t_1]}, \frac{\hbar}{i} \delta_{\alpha 3} \frac{\delta}{\delta J_a^\alpha[t_1]} \right]}_{\text{term 1}} \right. \right. \\ &\quad \left. \left. + \underbrace{\frac{-i}{\hbar} \delta_{a2} L_1 \left[\frac{\hbar}{-i} \delta_{\alpha 1} \frac{\delta}{\delta J_a^\alpha[t_1]}, \frac{\hbar}{-i} \delta_{\alpha 2} \frac{\delta}{\delta J_a^\alpha[t_1]}, \frac{\hbar}{-i} \delta_{\alpha 3} \frac{\delta}{\delta J_a^\alpha[t_1]} \right]}_{\text{term 2}} \right) \right] Z_0[J] \end{aligned} \quad (\text{D1})$$

with

$$Z_0[J] = e^{\frac{1}{2} \int_{t_i}^{t_f} dt_1 \int_{t_i}^{t_f} dt_2 J_b^\beta[t_1] G_{bc}^{\beta\gamma}[t_1, t_2] J_c^\gamma[t_2]}$$

where the Greek indices run from 1 to 3, and index the three cartesian coordinates. Consider a perturbing Lagrangian of the form

$$L_1 = -m\phi_g[x, y, z]$$

The 3D Taylor series expansion of $\phi_g[x, y, z]$ in position coordinates can be written in two different ways

$$\begin{aligned} \phi_g[x, y, z] &= \sum_{n=0}^{\infty} \frac{1}{n!} \Gamma_{\alpha_1 \alpha_2 \dots \alpha_n}^{(n-1)} r_{\alpha_1} r_{\alpha_2} \dots r_{\alpha_n} \\ &= \sum_{n_x=0}^{\infty} \sum_{n_y=0}^{\infty} \sum_{n_z=0}^{\infty} \frac{1}{n_x! n_y! n_z!} c_{n_x, n_y, n_z} x^{n_x} y^{n_y} z^{n_z} \end{aligned} \quad (\text{D2})$$

where repeating Greek indices are summed, and $x = r_1, y = r_2, z = r_3$. The Taylor series coefficients Γ are symmetric about an exchange of indices (for example, $\Gamma_{1,1,2} = \Gamma_{1,2,1} = \Gamma_{2,1,1} = c_{2,1,0}$, and $\Gamma_{1,2,3} = \Gamma_{1,3,2} = \Gamma_{2,1,3} = \Gamma_{2,3,1} = \Gamma_{3,1,2} = \Gamma_{3,2,1} = c_{1,1,1}$) since the position operators about the different dimensions commute with one another. The first equality of Eq. (D2) is adopting the notational conventions of [75], and it happens that expressing the diagram rules in terms of the Γ coefficients leads to simpler expressions. The second approach to expressing the Taylor series expansion, however, leads to a easier calculation of quantum corrections to atom interferometer phase shifts to first order in $\phi_g[x, y, z]$. The two approaches to Taylor expanding $\phi_g[x, y, z]$ leads to two different approaches to assigning value to diagram elements. The first one is

$$\begin{aligned}
& \begin{array}{c} \alpha_1 \\ \alpha_2 \\ \alpha_3 \\ \vdots \end{array} \left. \begin{array}{c} \text{---} \\ \text{---} \\ \text{---} \\ \vdots \end{array} \right\} n \text{ edges} \\
& \begin{array}{c} t, a \\ \vdots \end{array} = -m\Gamma_{\alpha_1\alpha_2\dots\alpha_n}^{(n-1)} \lambda_a^n \int_{t_i}^{t_f} dt \\
& \text{---} \overset{\alpha}{\text{---}} t, a = G_a^\alpha[t] \\
& t_1, a \overset{\alpha}{\text{---}} \text{---} \overset{\beta}{\text{---}} t_2, b = G_{ab}^{\alpha\beta}[t_1, t_2]
\end{aligned}$$

which is indicated in the main text Sec. II C. The alternate way to assign value to the diagrams is to label the diagram edges with the cartesian coordinate, and explicitly write out all the permutations over the cartesian coordinates as independent diagrams. In this approach, the various diagram vertices and edges values have values given by

$$\begin{aligned}
& \begin{array}{c} n_x \text{ x-edges} \\ \vdots \\ x \\ \vdots \\ y \\ \vdots \\ z \end{array} \left. \begin{array}{c} \text{---} \\ \text{---} \\ \text{---} \\ \vdots \end{array} \right\} n_y \text{ y-edges} \\
& \begin{array}{c} t, a \\ \vdots \end{array} = c_{n_x, n_y, n_z} \lambda_a^{n_x+n_y+n_z} \int_{t_i}^{t_f} dt \\
& \text{---} \overset{x}{\text{---}} t, a = G_a^1[t] \\
& \text{---} \overset{y}{\text{---}} t, a = G_a^2[t] \\
& \text{---} \overset{z}{\text{---}} t, a = G_a^3[t] \\
& t_1, a \overset{x}{\text{---}} \text{---} \overset{x}{\text{---}} t_2, b = G_{ab}^{11}[t_1, t_2] \\
& t_1, a \overset{y}{\text{---}} \text{---} \overset{y}{\text{---}} t_2, b = G_{ab}^{22}[t_1, t_2] \\
& t_1, a \overset{z}{\text{---}} \text{---} \overset{z}{\text{---}} t_2, b = G_{ab}^{33}[t_1, t_2]
\end{aligned}$$

where one must be careful about setting the correct symmetry factor given that the symmetry of the diagram needs to include symmetries associated with the cartesian indexes. The first approach to writing the diagram rules in 3D can be thought of as encoding the summation over all the diagrams, which have the same topology but differently labeled edges, in terms of the sum over Greek indices. When evaluating individual diagrams in 3D, it is productive to leverage the first form of the Taylor series expansion, so that the total number of diagrams required to compute perturbative corrections is minimized, but when computing general rules for the first order corrections to an arbitrary potential, the second expansion is more computationally convenient. In this section, we will express the external potential as a Taylor series of the first form, and when computing the leading order corrections to a potential with arbitrary spatial dependence in Sec.E, we will use the second form. We will now derive the vertex value for the case of expressing the Taylor series of $\phi_g[x, y, z]$ in terms of the Γ coefficients.

Consider the following perturbation to the system Lagrangian

$$L_1 = -\frac{1}{n!} m \Gamma_{\alpha\beta\gamma\dots}^{(n-1)} \underbrace{r_\alpha r_\beta r_\gamma \dots}_n$$

As in the 1D case of Sec. B, the tree level 1-vertex diagram here will come from the first order expansion of the functional, and the n^{th} order Taylor series expansion of Z_0 in Eq. (D1). We will first consider the contribution of just the ‘term 1’ of the functional in Eq. (D1). This Taylor series coefficients can be written as

$$\left(\epsilon \int_{t_i}^{t_f} dt \frac{i}{\hbar} \delta_{a1} \frac{1}{n!} \left(-m \Gamma_{\alpha_1\alpha_2\dots\alpha_n}^{(n-1)} \right) \left(\frac{\hbar}{i} \right)^n \frac{\delta}{\delta J_a^{\alpha_n}[t]} \dots \frac{\delta}{\delta J_a^{\alpha_2}[t]} \frac{\delta}{\delta J_a^{\alpha_1}[t]} \right) \left(\frac{1}{n!} \left(\frac{1}{2} \int_{t_i}^{t_f} dt_1 \int_{t_i}^{t_f} dt_2 J_{b_1}^{\beta_1}[t_1] G_{b_1 b_2}^{\beta_1 \beta_2}[t_1, t_2] J_{b_2}^{\beta_2}[t_2] \right)^n \right)$$

where

$$\frac{\delta}{\delta J_a^\alpha[t_2]} J_b^\beta[t_1] = \delta[t_1 - t_2] \delta_{ab} \delta_{\alpha\beta}$$

Applying the first functional derivative (the one with respect to $J_a^{\alpha_1}[t]$) gives us

$$\left(\epsilon \int_{t_i}^{t_f} dt \delta_{a1} \frac{1}{n!} \left(-m \Gamma_{\alpha_1 \alpha_2 \dots \alpha_n}^{(n-1)} \right) \left(\frac{\hbar}{i} \right)^{n-1} \frac{\delta}{\delta J_a^{\alpha_n}[t]} \dots \frac{\delta}{\delta J_a^{\alpha_2}[t]} \right) \\ \times \left(\frac{1}{n! 2^n} \underbrace{\left(\int_{t_i}^{t_f} dt_1 \int_{t_i}^{t_f} dt_2 J_{b_1}^{\beta_1}[t_1] G_{b_1 b_2}^{\beta_1 \beta_2}[t_1, t_2] J_{b_2}^{\beta_2}[t_2] \right)^{n-1}}_{\text{factor 1}} \underbrace{2n \left(\int_{t_i}^{t_f} dt_3 J_{b_3}^{\beta_3}[t_3] G_{b_3 a}^{\beta_3 \alpha_1}[t_3, t] \right)}_{\text{factor 2}} \right)$$

Then defining

$$G_a^\beta[t] = \int_{t_i}^{t_f} dt' J_{a'}^{\beta'}[t'] G_{a'a}^{\beta'\beta}[t', t]$$

we can simplify the notation of ‘factor 2’, and write the result of the application of all n functional derivatives (where we only apply the functional derivatives to the terms inside of ‘factor 1’ rather than ‘factor 2’ so as to build only the corresponding tree-level diagram) as

$$\left(\epsilon \int_{t_i}^{t_f} dt \delta_{a1} \frac{1}{n!} \left(-m \Gamma_{\alpha_1 \alpha_2 \dots \alpha_n}^{(n-1)} \right) \left(\frac{\hbar}{i} \right)^{n-1} \right) (G_a^{\alpha_1}[t] G_a^{\alpha_2}[t] \dots G_a^{\alpha_n}[t])$$

including the contributions of ‘term 2’ in the functional of Eq. (D1), the full tree level diagram can be written as

$$\underbrace{\frac{1}{n!}}_{\text{SYM}} \underbrace{\lambda_a^n \left(-m \Gamma_{\alpha_1 \alpha_2 \dots \alpha_n}^{(n-1)} \right)}_{\text{VERTEX}} \int_{t_i}^{t_f} dt \underbrace{G_a^{\alpha_1}[t] G_a^{\alpha_2}[t] \dots G_a^{\alpha_n}[t]}_{\text{EDGE}}$$

with

$$\lambda_a^n = \epsilon \left(\left(\frac{\hbar}{i} \right)^{n-1} \delta_{a1} + \left(\frac{\hbar}{-i} \right)^{n-1} \delta_{a2} \right)$$

Appendix E: Summing Over All 1-Vertex Diagrams in 3D

Consider a perturbative Lagrangian of the form

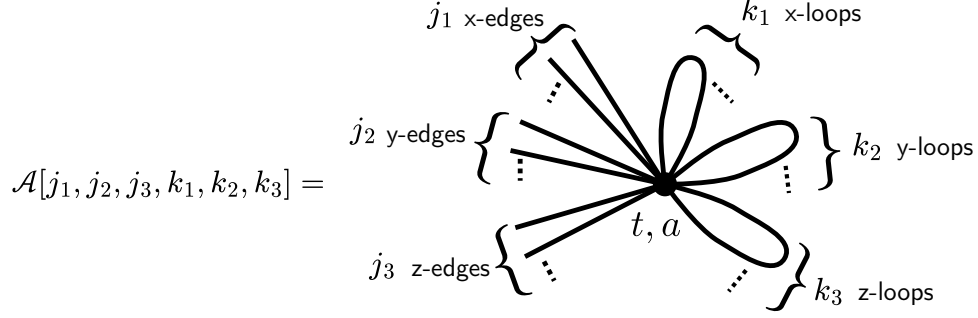
$$L_1[x, y, z] = -m \phi_g[x, y, z]$$

where ϕ_g can be written in terms of it’s Taylor series coefficients as

$$\phi_g[x, y, z] = \sum_{n_x=0}^{\infty} \sum_{n_y=0}^{\infty} \sum_{n_z=0}^{\infty} \frac{1}{n_x! n_y! n_z!} c_{n_x, n_y, n_z} x^{n_x} y^{n_y} z^{n_z}$$

In this paper, we will consider a gravitational external potential $\phi_g[\mathbf{r}]$, although the response to a general potential $V[\mathbf{r}]$ (originating from non-gravitational sources like inhomogeneous B fields or optical potentials) could also be computed by setting $\phi_g[x, y, z] = V[x, y, z]/m$. We will make the same simplifying assumptions as has been made

throughout the paper that the unperturbed Lagrangian L_0 can be written separably in terms of an x -, y -, and z -dependent x -dependent, component, $L_0[x, \dot{x}, y, \dot{y}, z, \dot{z}] = L_{0,x}[x, \dot{x}] + L_{0,y}[y, \dot{y}] + L_{0,z}[z, \dot{z}]$. A diagram with j_x x external edges, j_y y external edges, j_z z external edges, k_x x loops, k_y y loops, and k_z z loops has value $\mathcal{A}[j_x, j_y, j_z, k_x, k_y, k_z]$, where



The value of this diagram can be written in terms of the symmetry factor (SYM), the value of the vertex ($VERT$), and the value of all the edges ($EDGE$), $\mathcal{A}[j_x, j_y, j_z, k_x, k_y, k_z] = (SYM)(VERT)(EDGE)$ with

$$SYM = \frac{1}{j_x! j_y! j_z! k_x! 2^{k_x} k_y! 2^{k_y} k_z! 2^{k_z}}$$

$$VERT = \lambda_a^n (-mc_{j_x+2k_x, j_y+2k_y, j_z+2k_z}) \int_{t_i}^{t_f} dt$$

$$EDGE = (G_a^1[t])^{j_x} (G_a^2[t])^{j_y} (G_a^3[t])^{j_z} (G_{aa}^{11}[t, t])^{k_x} (G_{aa}^{22}[t, t])^{k_y} (G_{aa}^{33}[t, t])^{k_z}$$

with

$$\lambda_a^n = \epsilon \left(\left(\frac{\hbar}{i} \right)^{n-1} \delta_{a1} + \left(\frac{\hbar}{-i} \right)^{n-1} \delta_{a2} \right)$$

Now let's write the summation over the Latin index a explicitly as

$$\mathcal{A}[j_x, j_y, j_z, k_x, k_y, k_z] = \mathcal{A}_1[j_x, j_y, j_z, k_x, k_y, k_z] + \mathcal{A}_2[j_x, j_y, j_z, k_x, k_y, k_z]$$

with

$$\mathcal{A}_a[j_x, j_y, j_z, k_x, k_y, k_z] = \frac{1}{j_x! j_y! j_z! k_x! 2^{k_x} k_y! 2^{k_y} k_z! 2^{k_z}} \epsilon \left(\frac{\hbar}{i(-1)^{a+1}} \right)^{j_x+j_y+j_z+2k_x+2k_y+2k_z-1} (-mc_{j_x+2k_x, j_y+2k_y, j_z+2k_z})$$

$$\times \int_{t_i}^{t_f} dt (G_a^1[t])^{j_x} (G_a^2[t])^{j_y} (G_a^3[t])^{j_z} (G_{aa}^{11}[t, t])^{k_x} (G_{aa}^{22}[t, t])^{k_y} (G_{aa}^{33}[t, t])^{k_z}$$

we can write this more compactly with $j_1 = j_x$, $j_2 = j_y$, $j_3 = j_z$, $k_1 = k_x$, $k_2 = k_y$, $k_3 = k_z$ as

$$\mathcal{A}_a[j_1, j_2, j_3, k_1, k_2, k_3]$$

$$= \frac{1}{\prod_{\ell=1}^3 j_\ell! k_\ell! 2^{k_\ell}} \epsilon \left(\frac{\hbar}{i(-1)^{a+1}} \right)^{-1+\sum_{\ell=1}^3 j_\ell+2k_\ell} (-mc_{j_1+2k_1, j_2+2k_2, j_3+2k_3}) \int_{t_i}^{t_f} dt \prod_{\ell=1}^3 (G_a^\ell[t])^{j_\ell} (G_{aa}^{\ell\ell}[t, t])^{k_\ell}$$

$$= \epsilon \left(\frac{\hbar}{i(-1)^{a+1}} \right)^{-1} (-mc_{j_1+2k_1, j_2+2k_2, j_3+2k_3}) \int_{t_i}^{t_f} dt \prod_{\ell=1}^3 \frac{1}{j_\ell!} \left(\frac{\hbar}{i(-1)^{a+1}} G_a^\ell[t] \right)^{j_\ell} \frac{1}{k_\ell! 2^{k_\ell}} (-\hbar^2 G_{aa}^{\ell\ell}[t, t])^{k_\ell}$$

The sum over the number of external edges can be written as

$$\left(\prod_{\ell=1}^3 \sum_{j_\ell=0}^{\infty} \right) \mathcal{A}_a[j_1, j_2, j_3, k_1, k_2, k_3] =$$

$$\epsilon \left(\frac{\hbar}{i(-1)^{a+1}} \right)^{-1} (-m) \int_{t_i}^{t_f} dt \left(\prod_{\ell=1}^3 \frac{1}{k_\ell! 2^{k_\ell}} (-\hbar^2 G_{aa}^{\ell\ell}[t, t])^{k_\ell} \sum_{j_\ell=0}^{\infty} \frac{1}{j_\ell!} \left(\frac{\hbar}{i(-1)^{a+1}} G_a^\ell[t] \right)^{j_\ell} \right) c_{j_1+2k_1, j_2+2k_2, j_3+2k_3}$$

Then we can use the identity

$$\left(\prod_{\ell=1}^3 \sum_{j_\ell=0}^{\infty} \frac{1}{j_\ell!} (r_\ell)^{j_\ell} \right) c_{j_1+2k_1, j_2+2k_2, j_3+2k_3} = \left(\prod_{\ell=1}^3 \partial_\ell^{2k_\ell} \sum_{j_\ell=0}^{\infty} \frac{1}{j_\ell!} (r_\ell)^{j_\ell} \right) c_{j_1, j_2, j_3}$$

$$= \left(\prod_{\ell=1}^3 \partial_\ell^{2k_\ell} \right) \phi_g[r_1, r_2, r_3]$$

where

$$r_1 = x, r_2 = y, r_3 = z$$

$$\partial_1 = \partial_x, \partial_2 = \partial_y, \partial_3 = \partial_z$$

to write

$$\left(\prod_{\ell=1}^3 \sum_{j_\ell=0}^{\infty} \right) \mathcal{A}_a[j_1, j_2, j_3, k_1, k_2, k_3] =$$

$$\epsilon \left(\frac{\hbar}{i(-1)^{a+1}} \right)^{-1} (-m) \int_{t_i}^{t_f} dt \left(\prod_{\ell=1}^3 \frac{1}{k_\ell! 2^{k_\ell}} (-\hbar^2 G_{aa}^{\ell\ell}[t, t])^{k_\ell} \partial_\ell^{2k_\ell} \right) \phi_g[r_1, r_2, r_3] \Big|_{r_\ell = \frac{\hbar}{i(-1)^{a+1}} G_a^\ell[t]}$$

now summing over the loops as well, we have

$$\left(\prod_{\ell=1}^3 \left(\sum_{j_\ell=0}^{\infty} \sum_{k_\ell=0}^{\infty} \right) \right) \mathcal{A}_a[j_1, j_2, j_3, k_1, k_2, k_3]$$

$$= \epsilon \left(\frac{\hbar}{i(-1)^{a+1}} \right)^{-1} (-m) \int_{t_i}^{t_f} dt \prod_{\ell=1}^3 \left(\sum_{k_\ell=0}^{\infty} \frac{1}{k_\ell!} \left(-\frac{\hbar^2}{2} G_{aa}^{\ell\ell}[t, t] \partial_\ell^2 \right)^{k_\ell} \right) \phi_g[r_1, r_2, r_3] \Big|_{r_\ell = \frac{\hbar}{i(-1)^{a+1}} G_a^\ell[t]}$$

$$= \epsilon \left(\frac{\hbar}{i(-1)^{a+1}} \right)^{-1} (-m) \int_{t_i}^{t_f} dt \left(\prod_{\ell=1}^3 e^{-\frac{\hbar^2}{2} G_{aa}^{\ell\ell}[t, t] \partial_\ell^2} \right) \phi_g[r_1, r_2, r_3] \Big|_{r_\ell = \frac{\hbar}{i(-1)^{a+1}} G_a^\ell[t]}$$

$$= \epsilon \left(\frac{\hbar}{i(-1)^{a+1}} \right)^{-1} (-m) \int_{t_i}^{t_f} dt \left(e^{-\frac{\hbar^2}{2} \sum_{\ell=1}^3 G_{aa}^{\ell\ell}[t, t] \partial_\ell^2} \right) \phi_g[r_1, r_2, r_3] \Big|_{r_\ell = \frac{\hbar}{i(-1)^{a+1}} G_a^\ell[t]}$$

So that the leading order correction to the interferometer phase shift from this arbitrary gravitational potential can be written as

$$\Delta\phi^{(1)} = \text{Im} \left[\sum_{a=1}^2 \left(\frac{\hbar}{i(-1)^{a+1}} \right)^{-1} (-m) \int_{t_i}^{t_f} dt \left(e^{-\frac{\hbar^2}{2} \sum_{\ell=1}^3 G_{aa}^{\ell\ell}[t, t] \partial_\ell^2} \right) \phi_g[r_1, r_2, r_3] \Big|_{r_\ell = \frac{\hbar}{i(-1)^{a+1}} G_a^\ell[t]} \right] \quad (\text{E1})$$

There are two ways to proceed with the evaluation of Eq. (E1). One is to express the result as a convolution integral in the x , y , and z coordinates, and the second is to Taylor expand the exponential inside of the integrand and compute the time integral order by order in that expansion by taking higher and higher order derivatives of the potential $\phi_g[r_1, r_2, r_3]$. We will find that when computing the response to proof mass potentials, this second approach will be more productive. We can express Eq. (E1) as a convolution integral as

$$\Delta\phi^{(1)} = \text{Im} \left[-i \frac{m}{\hbar} \int_{t_i}^{t_f} dt \left(\bar{\phi}_g \left[\frac{\hbar}{i} G_1^1[t], \frac{\hbar}{i} G_1^2[t], \frac{\hbar}{i} G_1^3[t] \right] - \bar{\phi}_g \left[\frac{\hbar}{-i} G_2^1[t], \frac{\hbar}{-i} G_2^2[t], \frac{\hbar}{-i} G_2^3[t] \right] \right) \right]$$

where

$$\bar{\phi}_g[x, y, z] = \int_{-\infty}^{\infty} dx' \int_{-\infty}^{\infty} dy' \int_{-\infty}^{\infty} dz' \left(\frac{1}{4\pi \left(-\frac{\hbar^2}{2} G_{aa}^{11}[t, t]\right)} \right)^{1/2} \left(\frac{1}{4\pi \left(-\frac{\hbar^2}{2} G_{aa}^{22}[t, t]\right)} \right)^{1/2} \left(\frac{1}{4\pi \left(-\frac{\hbar^2}{2} G_{aa}^{33}[t, t]\right)} \right)^{1/2} \\ \times e^{-\frac{(x-x')^2}{4\left(-\frac{\hbar^2}{2} G_{aa}^{11}[t, t]\right)}} e^{-\frac{(y-y')^2}{4\left(-\frac{\hbar^2}{2} G_{aa}^{22}[t, t]\right)}} e^{-\frac{(z-z')^2}{4\left(-\frac{\hbar^2}{2} G_{aa}^{33}[t, t]\right)}} \phi_g[x', y', z']$$

where, including the harmonic components as part of the unperturbed Lagrangian L_0 , we have

$$G_{11}^{\ell\ell}[t, t] = G_{22}^{\ell\ell}[t, t] = -\frac{1}{2m\hbar} \left(\frac{1}{\beta_\ell} \cos[\omega_\ell(t-t_i)]^2 + \frac{\beta_\ell}{\omega_\ell^2} \sin[\omega_\ell(t-t_i)]^2 \right)$$

When the initial wavepacket waist is the ground state of the harmonic oscillator, we have

$$\beta_\ell = \frac{2\hbar}{m(w_{0,\ell})^2} \\ (w_{0,\ell})^2 = \frac{2\hbar}{m\omega_\ell} \\ \beta_\ell = \omega_\ell$$

in which case the functions $G_{aa}^{\ell\ell}[t, t]$ become time-independent

$$G_{11}^{\ell\ell}[t, t] = G_{22}^{\ell\ell}[t, t] = -\frac{1}{2m\hbar} \frac{1}{\omega_\ell}$$

When the harmonic components are not included as part of L_0 , the $G_a^\alpha[t]$ functions take the form of

$$G_a^1[t] = (-1)^{a+1} \frac{i}{\hbar} x_{\text{cl},a}^{(0)}[t] \quad G_a^2[t] = (-1)^{a+1} \frac{i}{\hbar} y_{\text{cl},a}^{(0)}[t] \quad G_a^3[t] = (-1)^{a+1} \frac{i}{\hbar} z_{\text{cl},a}^{(0)}[t]$$

and the $G_{aa}^{\alpha\alpha}[t, t]$ functions that the form

$$G_{11}^{\alpha\alpha}[t_1, t_2] = G_{22}^{\alpha\alpha}[t_1, t_2] = -\frac{1}{2m\hbar} \left(\beta_\alpha t^2 + \frac{1}{\beta_\alpha} \right)$$

in which case, the first order correction to the interferometer phase can be expressed as

$$\Delta\phi^{(1)} = -\frac{m}{\hbar} \int_{t_i}^{t_f} dt \left(\bar{\phi}_g \left[x_{\text{cl},1}^{(0)}[t], y_{\text{cl},1}^{(0)}[t], z_{\text{cl},1}^{(0)}[t] \right] - \bar{\phi}_g \left[x_{\text{cl},2}^{(0)}[t], y_{\text{cl},2}^{(0)}[t], z_{\text{cl},2}^{(0)}[t] \right] \right) \quad (\text{E2})$$

with

$$\bar{\phi}_g[x, y, z] = \int_{-\infty}^{\infty} dx' \int_{-\infty}^{\infty} dy' \int_{-\infty}^{\infty} dz' \left(\frac{1}{\pi \frac{\hbar}{m} (\beta_1 t^2 + 1/\beta_1)} \right)^{1/2} \left(\frac{1}{\pi \frac{\hbar}{m} (\beta_2 t^2 + 1/\beta_2)} \right)^{1/2} \left(\frac{1}{\pi \frac{\hbar}{m} (\beta_3 t^2 + 1/\beta_3)} \right)^{1/2} \\ \times e^{-\frac{(x-x')^2}{\frac{\hbar}{m} (\beta_1 t^2 + 1/\beta_1)}} e^{-\frac{(y-y')^2}{\frac{\hbar}{m} (\beta_2 t^2 + 1/\beta_2)}} e^{-\frac{(z-z')^2}{\frac{\hbar}{m} (\beta_3 t^2 + 1/\beta_3)}} \phi_g[x', y', z']$$

The alternative way of computing the right hand side of Eq. (E1) is to Taylor expand the exponential in the integrand. This is the approach we will take to making predictions for quantum corrections to proof mass potentials (see Sec. F), but this approach is also useful for seeing the fact that when the wavepacket is prepared with spherical symmetry, the quantum corrections vanish if the external potential satisfies Laplace's equation. Consider a system for which

$$G_{aa}^{11}[t, t] = G_{aa}^{22}[t, t] = G_{aa}^{33}[t, t]$$

Such a system could be one in which the initial wavefunction is spherically symmetric ($w_{0,x} = w_{0,y} = w_{0,z}$). Let us also consider the case that the harmonic term is not included as part of the unperturbed potential. In such a case, the integrand on the right hand side of Eq. (E1) can be written as

$$\begin{aligned} \left(e^{-\frac{\hbar^2}{2} \sum_{\ell=1}^3 G_{aa}^{\ell\ell}[t,t] \partial_\ell^2} \right) \phi_g[r_1, r_2, r_3] \Big|_{r_\ell = \frac{\hbar}{i(-1)^{a+1}} G_a^\ell[t]} &= \left(e^{-\frac{\hbar^2}{2} G_{aa}^{11}[t,t] \sum_{\ell=1}^3 \partial_\ell^2} \right) \phi_g[r_1, r_2, r_3] \Big|_{r_\ell = \frac{\hbar}{i(-1)^{a+1}} G_a^\ell[t]} \\ &= \left(e^{-\frac{\hbar^2}{2} G_{aa}^{11}[t,t] \nabla^2} \right) \phi_g[r_1, r_2, r_3] \Big|_{r_\ell = \frac{\hbar}{i(-1)^{a+1}} G_a^\ell[t]} \\ &= \left(1 - \frac{\hbar^2}{2} G_{aa}^{11}[t,t] \nabla^2 + \frac{1}{2} \left(-\frac{\hbar^2}{2} G_{aa}^{11}[t,t] \nabla^2 \right)^2 + \dots \right) \phi_g[r_1, r_2, r_3] \Big|_{r_\ell = \frac{\hbar}{i(-1)^{a+1}} G_a^\ell[t]} \end{aligned}$$

Where in the last line, we Taylor expand the exponentiated Laplace operator ∇^2 . The zeroth-order term yields the semiclassical approximation, and the higher-order terms (proportional to increasing powers of \hbar) represent increasingly higher-order quantum corrections. When $\nabla^2 \phi_g = 0$ (i.e. when the external potential satisfies Laplace's equation, as is the case for gravitational potentials in regions free of mass) every term beyond zeroth order in this expansion vanishes. Therefore, to first order in ϕ_g , there are no quantum corrections to the interferometer phase shift.

Appendix F: Details of Calculation of Response to Proof Mass Potential in 3D

It is difficult to express the solution $\phi_g[x, y, z]$ to Poisson's equation for the 'hollow cylinder' proof mass geometry indicated in Sec. IV C, in closed form for all spatial dimensions x , y , and z . Solving just along z , though ($\phi_g[0, 0, z]$), is more straightforward. The general solution to Poisson's equation for a gravitational potential is given by

$$\phi_g[\mathbf{r}] = -G \int d^3\mathbf{r}' \frac{\rho[\mathbf{r}']}{|\mathbf{r} - \mathbf{r}'|}$$

where $\rho[\mathbf{r}]$ is the density of the proof mass, and G is Newton's gravitational constant. Expressed in cylindrical coordinates, for a hollow cylinder proof mass potential with perfectly homogeneous mass density ρ_g , we have

$$\phi_g[0, 0, z] = -G \int_0^{2\pi} d\phi' \int_a^b ds' \int_{-L}^L dz' s' \frac{\rho_g}{\sqrt{(s')^2 + (z - z')^2}}$$

Where z is the axial coordinate, s is the radial coordinate, and ϕ is the azimuthal coordinate, and the origin of this coordinate system is the center-of-mass of the proof mass. The cylinder length is $2L$, the inner radius is a , and the outer radius is b , and the axis of cylindrical symmetry of the cylinder is collinear with the interferometer axis z . Evaluating these integrals gives us

$$\begin{aligned} \phi_g[0, 0, z] = & -G\pi\rho_g \left((L - z) \left(\sqrt{b^2 + (L - z)^2} - \sqrt{a^2 + (L - z)^2} \right) + (L + z) \left(\sqrt{b^2 + (L + z)^2} - \sqrt{a^2 + (L + z)^2} \right) \right) \\ & + b^2 \left(\log \left[(z + L) + \sqrt{b^2 + (L + z)^2} \right] - \log \left[(z - L) + \sqrt{b^2 + (L - z)^2} \right] \right) \\ & - a^2 \left(\log \left[(z + L) + \sqrt{a^2 + (L + z)^2} \right] - \log \left[(z - L) + \sqrt{a^2 + (L - z)^2} \right] \right) \end{aligned}$$

where G is Newton's gravitational constant, and ρ_g is the mass density of the proof mass. Assuming the gravitational potential is even in the radial coordinate $r^2 = x^2 + y^2$, we can write the general solution to $\phi_g[x, y, z]$ perturbatively in r as

$$\phi_g[x, y, z] = \phi_g^{(0)}[z] + \phi_g^{(2)}[z](x^2 + y^2) + \phi_g^{(4)}[z](x^2 + y^2)^2 + \phi_g^{(6)}[z](x^2 + y^2)^3 + \dots \quad (\text{F1})$$

Where $\phi_g[0, 0, z] = \phi_g^{(0)}[z]$. It happens that in order for ϕ_g to satisfy the Laplace equation $\nabla^2 \phi_g = 0$ (for the mass-free regions), the functions $\phi^{(n)}[z]$ must satisfy

$$\phi_g^{(n)}[z] = -\frac{1}{n^2} \partial_z^2 \phi_g^{(n-2)}[z]$$

So that given our solution to $\phi_g^{(0)}[z]$, we can build up solutions to $\phi_g^{(n)}[z]$ up from $n = 0$. Solving the recursive relationship above in order to express $\phi_g^{(n)}[z]$ in terms of $\phi_g^{(0)}[z]$, we have

$$\phi_g^{(2m)}[z] = (-1)^m \frac{1}{4^m (m!)^2} \partial_z^{2m} \phi_g^{(0)}[z] \quad (\text{F2})$$

Looking at the expansion of $\phi_g[x, y, z]$ in Eq. (F1), we can isolate the value of $\phi_g^{(n)}[z]$ for constant n by taking derivatives in the radial coordinate and setting the radial coordinate to zero.

$$(\partial_\perp^2)^{n_\perp} \phi_g[x, y, z] \Big|_{x=y=0} = 4^{n_\perp} (n_\perp!)^2 \phi_g^{(2n_\perp)}[z]$$

where $\partial_\perp^2 = \partial_x^2 + \partial_y^2$. We can express the right hand side in terms of $\phi_g^{(0)}[z]$ using Eq. (F2) as

$$(\partial_\perp^2)^{n_\perp} \phi_g[x, y, z] \Big|_{x=y=0} = (-1)^{n_\perp} \partial_z^{2n_\perp} \phi_g^{(0)}[z] \quad (\text{F3})$$

Now consider a case where the unperturbed Lagrangian does not include harmonic terms, and that the semiclassical trajectories associated with the wavefunctions of both arms stay along the interferometer (z) axis, such that the initial kinematics about the transverse dimensions are zero ($x_0 = y_0 = v_x = v_y = 0$). Let us also make the assumption that the initial wavepacket waist about the transverse coordinates are equal to one another. In this case, we have

$$\begin{aligned} w_{0,x} &= w_{0,y} = w_{0,\perp} \\ \beta_x &= \beta_y = \beta_\perp = \frac{2\hbar}{m(w_{0,\perp})^2} \\ G_{ab}^{11}[t_1, t_2] &= G_{ab}^{22}[t_1, t_2] = G_{ab}^\perp[t_1, t_2] \\ G_{11}^\perp[t, t] &= G_{22}^\perp[t, t] = -\frac{1}{2m\hbar} \left(\beta_\perp t^2 + \frac{1}{\beta_\perp} \right) \\ G_{11}^{33}[t, t] &= G_{22}^{33}[t, t] = -\frac{1}{2m\hbar} \left(\beta_3 t^2 + \frac{1}{\beta_3} \right) \end{aligned}$$

with $\beta_3 = 2\hbar / (m(w_{0,z})^2)$. We will assume that there are no semiclassical kinematics in the perpendicular dimensions

$$\begin{aligned} G_a^1[t] &= G_a^2[t] = 0 \\ G_a^3[t] &= \frac{i}{\hbar} (-1)^{a+1} z_{\text{cl},a}^{(0)}[t] \end{aligned}$$

in this case, Eq. (E1) becomes

$$\Delta\phi^{(1)} = \sum_{a=1}^2 \left(\frac{\hbar}{(-1)^{a+1}} \right)^{-1} \int_{t_i}^{t_f} dt \left. e^{-\frac{\hbar^2}{2} G_{aa}^\perp[t,t] \partial_\perp^2} e^{-\frac{\hbar^2}{2} G_{aa}^{33}[t,t] \partial_z^2} \phi_g[x, y, z] \right|_{\substack{x=y=0 \\ z=z_{\text{cl},a}^{(0)}[t]}}$$

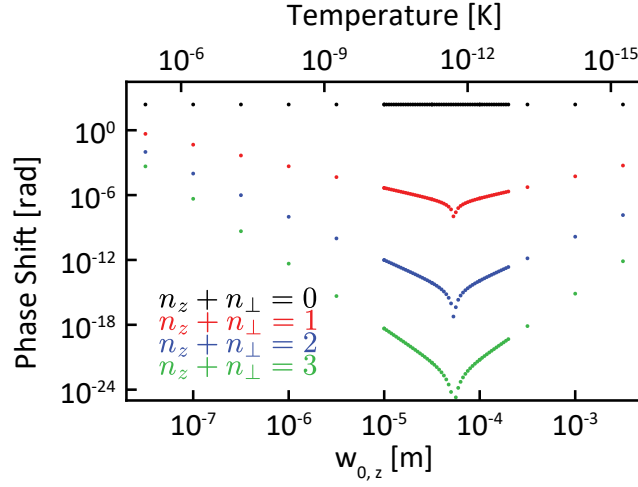


FIG. 7. The absolute value of semiclassical and quantum corrections to the atom interferometer phase shift for the interferometer sequence described in Sec. IV C. The semiclassical solutions are written black, the leading order quantum contributions are in red, the second order corrections are in blue, and the third order corrections are in green. The quantum corrections indicated in Fig. 6 are dominated by the leading order quantum corrections (red). For each value of n_z , n_\perp , and $w_{0,z}$, we numerically evaluate the integral over time associated with Eq. (F4). We take the radial waist $w_{0,\perp}$ to scale with the longitudinal waist $w_{0,z}$ as $w_\perp = w_{0,z}/\sqrt{2}$.

Taylor expanding the exponentials gives us

$$\Delta\phi^{(1)} = \sum_{a=1}^2 \left(\frac{\hbar}{(-1)^{a+1}} \right)^{-1} \int_{t_i}^{t_f} dt \sum_{n_\perp=0}^{\infty} \sum_{n_z=0}^{\infty} \frac{1}{n_\perp!} \frac{1}{n_z!} \left(-\frac{\hbar^2}{2} G_{aa}^\perp[t, t] \right)^{n_\perp} \left(-\frac{\hbar^2}{2} G_{aa}^{33}[t, t] \right)^{n_z} \partial_\perp^{2n_\perp} \partial_z^{2n_z} \phi_g[x, y, z] \Big|_{\substack{x=y=0 \\ z=z_{\text{cl},a}^{(0)}[t]}}$$

We can express this in terms of derivatives applied to $\phi^{(0)}[z]$ using Eq. (F3)

$$\partial_\perp^{2n_\perp} \partial_z^{2n_z} \phi_g[x, y, z] \Big|_{\substack{x=y=0 \\ z=z_{\text{cl},a}^{(0)}[t]}} = \partial_z^{2n_z} \left(\partial_\perp^{2n_\perp} \phi_g[x, y, z] \Big|_{x=y=0} \right) \Big|_{z=z_{\text{cl},a}^{(0)}[t]} = (-1)^{n_\perp} \partial_z^{2(n_\perp+n_z)} \phi_g^{(0)}[z] \Big|_{z=z_{\text{cl},a}^{(0)}[t]}$$

Our first order correction to the interferometer phase shift can therefore be expressed purely in terms of derivatives of $\phi_g^{(0)}[z]$ as

$$\Delta\phi^{(1)} = \sum_{a=1}^2 \left(\frac{\hbar}{(-1)^{a+1}} \right)^{-1} \int_{t_i}^{t_f} dt \sum_{n_\perp=0}^{\infty} \sum_{n_z=0}^{\infty} \frac{1}{n_\perp!} \frac{1}{n_z!} \left(-\frac{\hbar^2}{2} G_{aa}^\perp[t, t] \right)^{n_\perp} \left(-\frac{\hbar^2}{2} G_{aa}^{33}[t, t] \right)^{n_z} (-1)^{n_\perp} \partial_z^{2(n_\perp+n_z)} \phi_g^{(0)}[z] \Big|_{z=z_{\text{cl},a}^{(0)}[t]} \quad (\text{F4})$$

For the experimental parameter of the 3D proof mass calculation, it happens that higher and higher orders of \hbar contribute more weakly (see Fig. 7). As part of the computation presented in Sec. IV C, we include orders up to $n_\perp + n_z = 3$ (i.e. summing over all values of n_z and n_\perp for which $n_\perp + n_z = 3$), where $n_\perp = n_z = 0$ is the semiclassical solution. The relative contribution for each of these orders for the parameters used to produce Fig. 6 are indicated in Fig. 7.